Engineering Structures 239 (2021) 112177

Contents lists available at ScienceDirect

Engineering Structures

journal homepage: www.elsevier.com/locate/engstruct

Key aspects in the analysis and design of Hyperloop™ infrastructure under static, dynamic and thermal loads

Pedro Museros, Carlos Lázaro *, Benjamín Pinazo, Salvador Monleón

Dpt. of Continuum Mechanics and Theory of Structures, Universitat Politècnica de València, Valencia 46022, Spain

ARTICLE INFO

Keywords:
Hyperloop
Civil constructions
Longitudinal thermal expansion
Stability
Structural dynamics
Moving loads
Continuous beams
High-speed

ABSTRACT

Hyperloop is an avant-garde idea for high-speed transportation of passengers and freight in a *pod* or capsule-like vehicle travelling through an hermetically sealed tube with reduced internal pressure. Its maximum envisaged speed is around 1200 km/h, which would be directly comparable to airplane travel and much faster than road and railway transportation. Because the unconventional, ad hoc civil infrastructure required for Hyperloop is still under a conceptual design phase, one of the most important steps to undertake at this stage is to develop analytical models and tools to simulate the mechanical behaviour, so that any potential issue can be anticipated. This article is a novel comprehensive study of the relevant phenomena that influence the design of Hyperloop infrastructure from the structural engineering viewpoint. The aim is to obtain, for the first time, representative values of the main internal forces and stresses leading to a preliminary design of the vacuum tube and, simultaneously, to provide relevant insight into the main phenomena involved. Depending on the longitudinal restrictions implemented at the piers, two basic configurations based on steel tubes are proposed. The strength and stability of the tube have been analysed thoroughly by taking into account the self and dead weight, internal low pressure, wind, thermal and traversing vehicle dynamic effects. Fatigue has also been assessed at potential critical locations. The relevance of each external action has been suitably highlighted, with particular emphasis on the predominant thermal and buckling effects. Estimates of the required tube thickness are provided, and resonance phenomena at some particular speeds are pointed out. Since the Hyperloop concept comprises both vehicle design and structure standardization that strongly relate to each other, their definition must be advanced in parallel. This work represents a starting point for future detailed studies, as the HL technology evolves through subsequent stages when relevant details of vehicle design will be available.

1. Introduction

Means of transport constitute an essential network for the development and functioning of human societies. Given their leading role in economic activity, different transport technologies are in continuous evolution within the framework of four different paradigms: road transport, aviation, naval transport and railway systems. However, in recent years a *fifth mode* of transport has entered the scene and demands increasing attention from both industry and academia: *Hyperloop*™, as a trademark of Elon Musk's *SpaceX* company, has been gaining focus since its coming out in 2013 [1]. Actually, the idea of a "train" travelling at very high speeds into a vacuum tube was first set out by an American rocket engineer, Robert Goddard, back in 1910. Regardless of its historical origins, the recent awakening of activity around Goddard's initial idea must be certainly attributed to the timely proposal of Musk: in present time there is an imprecise, yet undeniable feeling that technology may be ready to make the dream of travelling on a train at the speed of an airplane come true.

A large number of news have been published since Musk's *Hyperloop Alpha* document was unveiled [1]. Some of them claimed that the advent of HL as a new means of transport is close to become reality by "integrating already proven technologies in a new way" [2]. Conversely, some others stated serious warnings about potential technical problems that could render the new vacuum tube-trains unfeasible [3]. A number of large consortia have been created in order to develop HL systems [2,4], also with a view to launching standardisation committees such as CEN-CLC/JTC 20 [5], and relevant companies such as Virgin, Leybold, ADIF, Arup or Deutsche Bahn have been involved into HL to different degrees, according to other news releases. Pod competitions organised by Musk have attracted researchers from many universities in different

* Corresponding author.
E-mail addresses: pmuseros@mes.upv.es (P. Museros), carlafer@mes.upv.es (C. Lázaro), bpinazo@doctor.upv.es (B. Pinazo), smonleon@mes.upv.es (S. Monleón).

https://doi.org/10.1016/j.engstruct.2021.112177
Received 9 July 2020; Received in revised form 14 February 2021; Accepted 4 March 2021
Available online 20 April 2021

countries, and several test facilities have been already built (*Virgin Hyperloop One* in Nevada, USA; *HyperloopTT* in Toulouse, France) or are planned for the near future (*HL Hardt* in Groningen, Netherlands; *Zeleros* in Sagunto, Spain). Whether this effervescence around HL will eventually result in a new paradigm for passengers and/or goods transportation, is still unknown. Feasibility studies and market analyses covering several regions worldwide have been carried out [2,6,7], but similar projects failed due to economic problems that their leaders could not get around, even if the initial stages of development were truly promising [8].

Nevertheless, the ongoing activity and the synergies built around the HL concept are relevant enough to deserve technical answers to the essential points of structural design. Among those points, the following questions are of principal importance: Is it possible to build the main HL infrastructure using standard civil engineering solutions? What will be the governing actions in the design? What would be the structural safety margins in a typical HL vacuum tube supported on piles? Will it be possible to suitably accommodate the stress/strain levels induced by thermal expansion in a continuous structure hundreds of kilometres long? Will the HL vehicles running at 1000 km/h create resonance vibration problems similar to modern high-speed trains, or even more severe?

Because the technology of HL vehicles, propulsion and guiding systems is still in constant evolution and many details are kept secret by different competitors, it is not yet possible to provide answers to *local* structural problems such as the union of levitation rails with the tube, welding details, etc. Instead, a gradual definition of the optimal solutions is to be expected as HL technology evolves through subsequent stages, with contributions arriving from many different areas of engineering. As a result, the present lack of definition of details steers the initial structural analysis to be carried out from a *global* perspective, to obtain representative values of the main internal forces and stresses for the preliminary design of the vacuum tube. This is, consequently, the principal objective of this paper.

The analysis of local details for the unions between tube and piers is also beyond the scope of the article, since definitive technological solutions for the tube structure are to be adopted first. In this regard, steel tubes are being used in the existing test facilities of Virgin Hyperloop One and HyperloopTT, but other structural solutions are being explored by some HL teams. In this paper research is focused on the use of steel tubes, which is a rational option in the present stage and will allow to obtain useful orders of magnitude of the main phenomena that influence design. Moreover, given that the characteristics of actual HL vehicle suspensions have not been disclosed by the main competitors, it is not feasible to carry out a detailed *Serviceability Limit State* analysis, which will be directly related to the levels of structural deformation and vibration that vehicles can withstand without malfunctioning or inducing passenger discomfort. Instead, the *Ultimate Limit State* (ULS) analysis can be tackled with sufficient guarantee for the steel tubular structure—except for the local details mentioned before.

From the point of view of structural analysis, the existing contributions to HL infrastructure design are very scarce. There seems to be a general agreement that a standard HL section is to be built on piers for optimising the economic investment [9], but even the most recent reports [2] do not discuss any relevant information about the essential structural demands: self-weight and wind loads, inner vacuum, thermal expansion and vehicle effects (including dynamic amplification factors and fatigue). This article endeavours to treat them all with suitable beam and shell theories, in a view to obtain maximum stress levels and analyse the tube behaviour. A typical case study is included; it provides useful orders of the principal magnitudes and dimensions involved.

Very few works have been published regarding the behaviour of HL infrastructure as a load-bearing system. In a pioneering work, Alexander and Kashani carried out a dynamic assessment of HL viaducts under a moving mass and pointed out the possibility of resonance phenomena caused by the vehicles travelling at supercritical speeds [10]. Later, Ahmadi in collaboration with the two previous authors undertook also an analysis of the HL tubes in lateral resonant oscillation, where the piers impose a transverse restrain as they undergo bending deformation [11]. Both references from this research team will be further commented in Section 9. Very recently, Connolly and Alves Costa investigated the geodynamic effects of very high-speed transport systems; they focus on the soil vibrations created by multiple loads moving at speeds above the critical soil velocity [12] and discuss some scenarios where strong resonance phenomena could adversely affect the underlying soil. Connolly and Alves Costa point out that probably some sections of the route will be constructed underground or very close to the soil's surface. There are good reasons to support such statement, but it is also true that some

Table 1
Table of symbols.

Symbols	Symbol Description
E, G, ν; f_y	Young modulus, shear modulus, Poisson ratio; yield stress
γ_s; α	specific weight; thermal expansion coefficient
l; d_{ext}, d; t	span length; tube external/middle diameter; tube thickness
A; I_y, I_z; $W_{el,y}$, $W_{el,z}$	tube section area; second moments of area; elastic section moduli
L; k	continuous viaduct semi-length; horizontal spring constant per unit length
ξ; λ_k	non-dimensional longitudinal coordinate; non-dimensional elastic slenderness
$T(\xi)$; ϵ_T; $N(\xi)$	temperature variation along axial direction; thermal strain, tube axial force
$f(\xi), f_u, f_{adm}$	distributed interaction force, max. due to unif. ΔT, max. admissible
u, u_u, u_a, u_{adm}	long. displacement, due to unif. ΔT, due to linear ΔT; max. admissible
a, l_r	cylinder radius, distance between contiguous ring stiffeners
C, D	shell membrane and flexural rigidities
m, n	number of half/full buckling waves in longitudinal/radial direction
p_{cr}	critical uniform radial pressure in a cylinder
R	ratio between the axial and circumferential membrane forces
$\sigma_{x,cr}, \sigma_{\theta,cr}$	critical longitudinal stress, critical hoop stress
Z, η, γ	tube curvature parameter (Batdorf), plasticity factor, correction factor
k_x, k_θ	buckling coefficient for axial compression/bending, for radial pressure
$g_{1,k}, g_{2,k}$; β	self, dead weight (characteristic values); dead to self weight ratio
p_k, F_k, w_k	internal vacuum, vehicle load, wind load (characteristic values)
η; $c_{f,z}, q_p$	impact factor (DAF); vertical wind force coefficient, peak wind velocity pressure
T_u; T_a, $-T_a$	uniform temperature increment; end temp. increments for long. gradient
T_{g+}, T_{g-}; $\chi_{k,T}$	upper temperature increments (heat, cool); vert. gradient induced curvature
γ_d; $\gamma_{G,i}, \gamma_{Q,i}$	security factor; safety coefficients
$\psi_{0,F}, \psi_{0,w}, \psi_{0,T}$	combination coefficients
k_c, k_a	Bending moment coefficient at midspan and adjacent support (Timoshenko)
$\sigma^p_{x,k}, \sigma^p_{\theta,k}$	characteristic values of longitudinal and hoop stresses due to vacuum
$\sigma^p_{x,d}, \sigma^p_{\theta,d}$	design values of longitudinal and hoop stresses due to vacuum
$\sigma^c_{x,d}, \sigma^b_{x,d}$	design values of longitudinal stress for compressive and bending loads
$\sigma_{VM,d}$	design values of equivalent von Mises stresses
$\sigma^c_{x,cr}, \sigma^b_{x,cr}, \sigma^p_{\theta,cr}$	critical stresses for compressive, bending and radial loads
$\Delta\sigma_L$	fatigue stress cut-off limit as per EN1993-1–9
γ_{Mf}, γ_{Ff}; λ_{max}	fatigue partial safety factors; damage equivalent factor
S_{stat}, S_{dyn}	maximum static effect, maximum dynamic effect - movement or internal forces
$\varphi_{dyn}{}', \varphi'', V_{crit}, \omega$	dynamic amplification, irregularity factor, critical speed, angular frequency

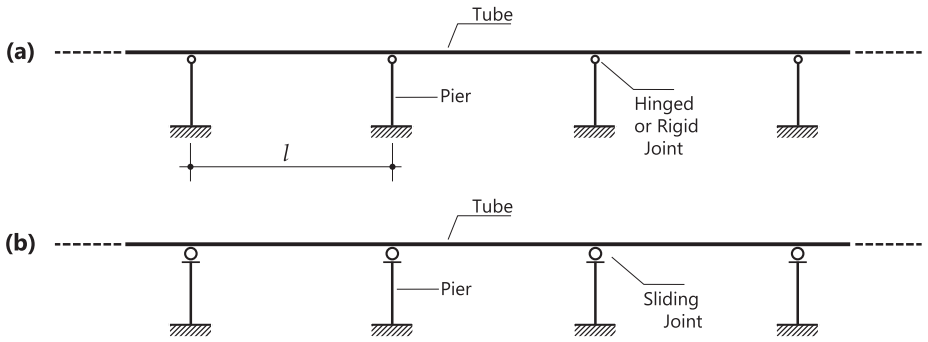

Fig. 1. Structural systems for Hyperloop viaducts of span lenght l in **(a) R-Configuration** (restrained axial expansion) and **(b) F-Configuration** (free axial expansion).

countries as Japan or, more recently, China, have developed a very large portion of their high-speed rail networks on viaducts [13]. For this reason, while it is undeniable that soil vibrations will be induced through the pier's foundations of HL viaducts that may affect the surrounding buildings, at the present stage it is necessary to carry out first a dynamic analysis where the main bending deformability of the tube is investigated. This will be the approach adopted for the dynamic assessment in this paper, in combination with a suitable treatment of the rest of mechanical/thermal actions.

Some other technical papers can be retrieved in scientific databases where various aspects of the HL system are described, as for instance, the recent research carried out by Nick and Sato to aid the development of an HL pod [14]. In such paper, three-dimensional compressible flow simulations were conducted featuring a novel usage of Gamma transition model, in which the switch from laminar to turbulent flow can be predicted. Despite advanced studies in various fields related to HL such as [14] are being published lately, no other relevant publications exist with an emphasis on the structural analysis and design except for the ones mentioned above. For such reason, the authors believe that the present article can serve as a first step towards a rational analysis of the mechanical behaviour and load-bearing capacity of HL vacuum tube systems.

Two possible main configurations of the tube are discussed first in Section 2. Then, the thermal effects are analysed for those configurations, followed by an examination of the conditions required by the stability under vacuum pressure (Sections 3 and 4). Both such effects play a major role in the design. Subsequently, the ULS assessment is carried out in Sections 5 (design load combinations), 6 (strength check) and 7 (stability check). A maximum *allowable impact coefficient* related to dynamic response will be derived in Section 7. The potential need of in-depth fatigue analysis will be discussed in Section 8, and Section 9 will deal with the essential dynamic phenomena associated to the behaviour of the tube as a beam. All conclusions will be illustrated with applications where typical design values will be considered. For the sake of conciseness, a number of abbreviations will be used throughout the paper[1]. A summary of the symbolic notation is given in Table 1.

2. Basic assumptions and modelling considerations

The typical Hyperloop viaduct consists of a steel tube (or pair of tubes) of constant thickness. We assume that the tube is self-supporting and works as a continuous beam on approximately equidistant supports (piers) with a typical span length l ranging between 20 and 40 m. In order to keep the discussion as general as possible, two basic configurations are considered, depending on whether the longitudinal displacements of the tube are constrained by the piers or not:

R-Configuration (restrained axial expansion): The tube is connected to the piers in the longitudinal and transverse directions. In principle, the tube-pier joints may be designed as hinged supports or as rigid or semi-rigid joints, in which case the relative rotation of the tube with respect to each pier would be also constrained. In this article hinged supports will be considered in the R-Configuration, where the thermal expansion of the tube is also constrained by the piers to a significant extent that depends on the stiffness of the pier-foundation system. Fig. 1 (a) shows the structural system for the R-Configuration. Regarding the tube, ring stiffeners are considered to be located at the support sections, as usual in cylindrical shells; they contribute to the tube buckling strength and help transferring loads to the pier. Intermediate ring stiffeners can be also arranged, although if nothing is specified, only the support stiffeners will be considered.

F-Configuration (free axial expansion): Unlike in R-Configuration, the tube can slide in longitudinal direction on each pier, so that thermal expansion is admitted to be free in this configuration. Lateral relative displacements are still constrained. Due to the lack of longitudinal constraints, uniform changes of temperature and longitudinal linear temperature gradients do not induce forces in the structure. Though the technology required for the free thermal expansion in F-Configuration is, as such, not developed yet, it is of interest to explore this possibility that was initially proposed in the form of a "telescoping tube" in [1] or "bellows system" in [2]. For long tubes (hundreds of km), longitudinal displacements in this configuration may be of the same order of magnitude as the typical span length, which precludes the arrangement of external ring stiffeners. Therefore, a non-stiffened tube is considered here, although internal stiffening might be an option to be explored at later stages (this option could have an influence in the air flow around the vehicle during operation at very high speeds). Fig. 1 (b) shows the structural system for the F-Configuration.

In both configurations, the vertical displacement of the tube is assumed to be fully restrained by the piers. Regarding the materials, we admit that the steel for the tube is Duplex (standard) EN 1.4462 (ASTM 2205) for its superior strength in comparison with conventional steels, as well as for its high corrosion resistance [15]; its specific weight is $\gamma_s = 78.0\,\text{kN/m}^3$, modulus of elasticity $E = 200\,\text{GPa}$, thermal expansion coefficient $\alpha = 1.3 \times 10^{-5}\,^{\circ}\text{C}^{-1}$ and yield stress $f_y = 460\,\text{MPa}$. Piers of standard concrete will be considered where appropriate. The possible use of S355 steel is discussed in Section 7.

The permanent and variable loads used for design (self-weight and dead load, temperature, vehicle, vacuum pressure and wind) are summarised in Section 5. Snow load and accidental loads such as the seismic action are not considered in this phase of the study.

Let d_{ext} and t be the outer diameter and thickness of the tube. According to Eurocode 3 [16], tubular sections where $d_{ext}/t > 90\varepsilon^2 = 90\sqrt{235\,\text{MPa}/f_y}$ ought to be analysed as a shell. Then, for Duplex EN 1.4462 steel, the HL tube is to be analysed as a shell whenever $t < d_{ext}/64.328$, which gives a thickness of 62 mm for $d_{ext} = 4.0$ m. It is

[1] Abbreviations: HL, Hyperloop™; ULS, Ultimate Limit State; SLS, Serviceability Limit State; VBI, vehicle-bridge interaction.

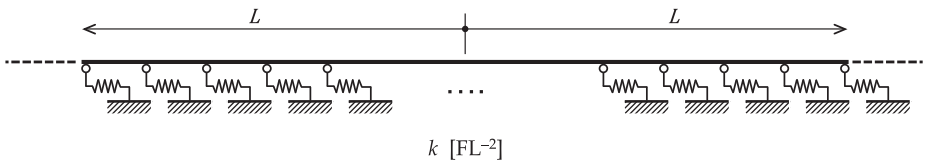

Fig. 2. Model for thermal analysis of the R-Configuration. Expansion is elastically restrained by a continuum of springs.

clear that for usual thicknesses that one should consider a priori in the design of a tubular structure for HL, shell behaviour can not be ignored in the analysis. This fact is taken into account thoughout the paper except for the dynamic analyses, where a refined shell approach falls outside the scope of the paper.

In what follows we admit that stresses can be obtained in linear analysis by superposition of the results of a beam model (that will take into account bending and longitudinal thermal expansion), and a shell model (that is able to capture the longitudinal and hoop stresses due to vacuum as well as to differential thermal expansion with the ring stiffeners at the supports). Additionally, we evaluate separately the effect of the uniform temperature change and the effect of other loads. The first one is modelled —in the case of the R-Configuration— with a bar restrained by a continuum of longitudinal springs (Section 3), whereas the transverse loads and the vertical temperature gradient act on a continuous beam on simple supports in both configurations (Section 6). The mechanical characteristics of the cross-section for the beam model are computed by neglecting the thickness in comparison to diameter d, which is referred to the medium line of the hollow tube: $A = \pi d t$ (area); $I_y = I_z = \frac{1}{8}\pi d^3 t$ (2nd moment of area); $W_{el,y} = W_{el,z} = 2\frac{I_z}{d} = \frac{\pi}{4} d^2 t$ (elastic section modulus).

3. Effect of thermal loads

One of the key aspects to analyse in the HL structural design is the effect of thermal expansion. The HL routes are intended to cover distances of hundreds of kilometres. A simple estimate of the unrestrained end displacement of a 600 km long steel tube (approx. distance from San Francisco to Los Angeles) under uniform temperature increase of the order of 50 °C yields values of about 200 m. This rises serious concerns about the feasibility of the tube in such conditions, and leads to conceive the HL system with *large expansion joints* located at certain intervals, in combination with supports at the piers that allow for free longitudinal movement of several meters. This is the scheme that has been described as *F-Configuration* in Section 2 and Fig. 1 (b). In this case the expansion joints would be of the "telescope" type initially mentioned in [1]. No thermal stresses would be induced in the tube.

A very different alternative is to consider that the piers will provide a relevant restriction to thermal expansion, so that longitudinal displacements will be much smaller while, in turn, there will be a significant level of thermal stress. This scheme was referred to as *R-Configuration* in Section 2 and Fig. 1 (a), and is similar to a long welded rail in a railway line, where the central part of each sector between expansion joints has restricted movements and high thermal stresses, while in the end parts of the sector a (limited) displacement is absorbed by *smaller expansion devices* and stresses drop to zero. In such case, the expansion "devices" or "joints" for HL will not need to accommodate a tube sliding of several meters, but much shorter movements.

In this section, the R-Configuration (restrained axial expansion) is analysed in detail for the first time. Suitable solutions are discussed in order to limit the displacements at the ends of each sector of restricted expansion.

3.1. Simplified model for the R-Configuration

A convenient approach for analysing the thermal problem from a global perspective is to idealise the continuous viaduct as a uniform bar of length $2L$ and axial rigidity EA, that is elastically restrained in the longitudinal (axial) direction by a continuum of linear elastic springs of constant k with physical dimensions FL^{-2} (see Fig. 2). We will refer to it later as the *interface stiffness*. Only stresses and strains in the axial direction x of the bar are considered. The thermal strain $\epsilon_T(x)$ is known *a priori*

$$\epsilon_T(x) = \alpha T(x) \tag{1}$$

where α is the thermal expansion coefficient and $T(x)$ is the temperature variation at each section of coordinate x, which is admitted to be uniform in the cross-section of the tube. Local equilibrium and superposition of the thermal strain plus the effect of the axial force are expressed as

$$\frac{\mathrm{d}N}{\mathrm{d}x} = -f(x), \qquad \frac{\mathrm{d}u}{\mathrm{d}x} = \epsilon_T(x) + \frac{N(x)}{EA} \tag{2}$$

where $N(x)$ is the axial force and the (unknown) distributed interaction force exerted by the spring-continuum in axial direction is

$$f(x) = -k u(x) \tag{3}$$

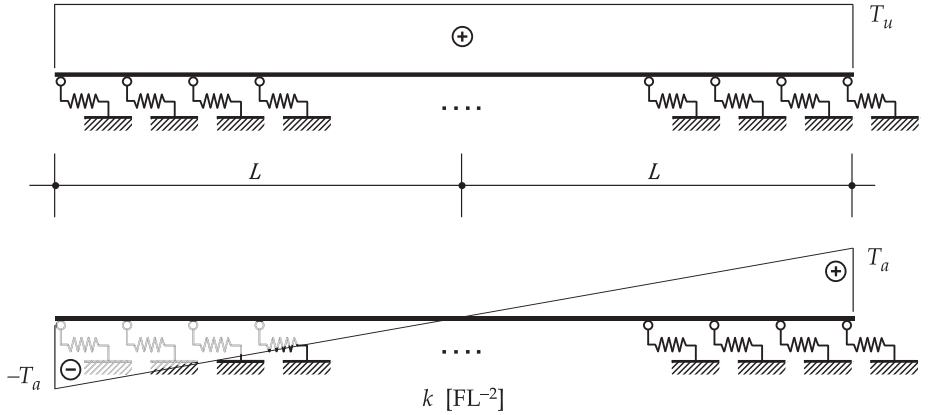

Fig. 3. Thermal action on the R-Configuration. Uniform increment (top); longitudinal gradient (bottom).

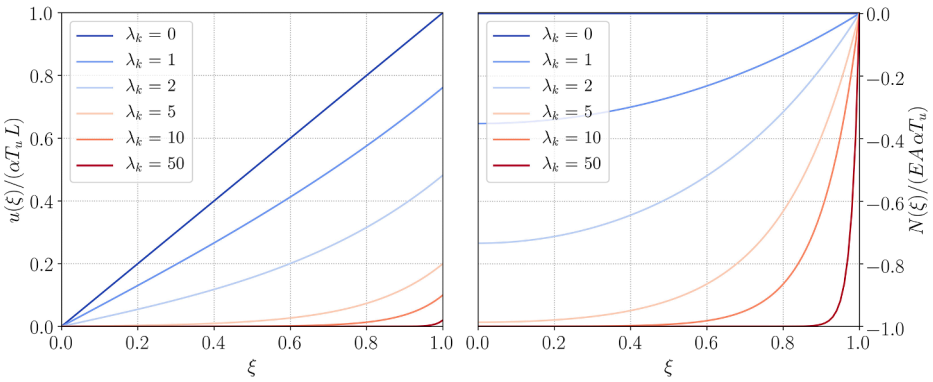

Fig. 4. Displacement (left) and normalised axial force (right) due to a uniform temperature increment, for different values of the elastic slenderness.

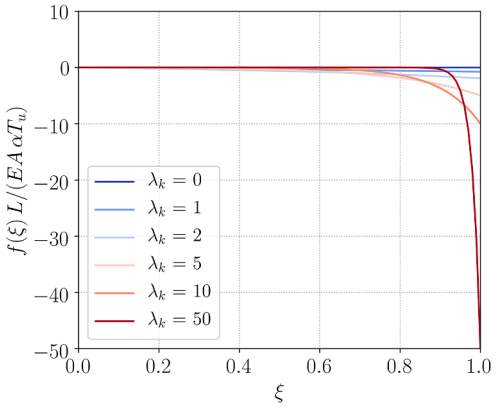

Fig. 5. Normalised interaction force due to a uniform temperature increment.

Combination of the previous expressions leads to the following equation

$$\frac{\mathrm{d}^2 u}{\mathrm{d}x^2} - \frac{k}{EA}\,u(x) = \frac{\mathrm{d}\epsilon_T}{\mathrm{d}x} \tag{4}$$

3.2. Uniform temperature increment

The solution of ordinary differential Eq. (4) for a uniform temperature increment T_u (Fig. 3) is

$$u(\xi) = \alpha T_u L\,\frac{1}{\lambda_k}\,\frac{\sinh(\lambda_k \xi)}{\cosh(\lambda_k)} \tag{5}$$

where $\xi = x/L$ is the non-dimensional independent variable and

$$\lambda_k = L\sqrt{\frac{k}{EA}} \tag{6}$$

is the non-dimensional *elastic slenderness* that measures the ratio of the elastic constraint to the axial rigidity. The details of the derivation can be found in Appendix A. The mid-point of the tube is $\xi = 0$, where displacement is zero due to symmetry. Substitution of (5) in (2) yields the axial force along the rod

$$N(\xi) = -EA\,\alpha T_u\left(1 - \frac{\cosh(\lambda_k \xi)}{\cosh(\lambda_k)}\right) \tag{7}$$

Displacements and axial forces for different values of the slenderness are represented in Fig. 4 in non-dimensional form. In general, axial forces could be positive or negative depending on the sign of the temperature variation $T(x)$.

The distributed *interaction force* (physical dimensions FL^{-1}) is given by the compatibility Eq. (3). The normalised value is represented in Fig. 5.

$$f(\xi) = -k\,u(\xi) = -\frac{EA\,\alpha T_u}{L}\lambda_k\,\frac{\sinh(\lambda_k \xi)}{\cosh(\lambda_k)} \tag{8}$$

3.3. Uniform temperature gradient between tube ends

An approach analogous to that in the previous section yields the solution to Eq. (4) when the tube is subjected to a uniform longitudinal gradient, *i.e.* a linear variation of temperature between $-T_a$ at $x = -L$ and T_a at $x = L$ (Fig. 3)

$$T(x) = T_a\,\frac{x}{L} \tag{9}$$

The solution for this case is included in Appendix A; the corresponding

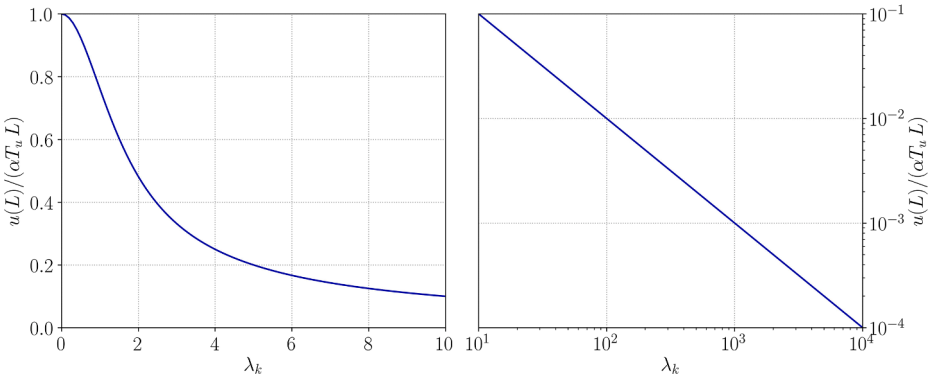

Fig. 6. Displacement of the end of the breathing length caused by a uniform temperature increment.

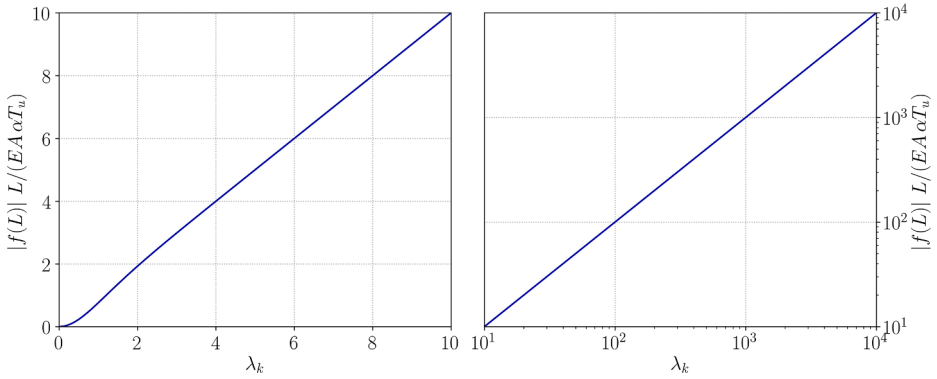

Fig. 7. Absolute value of the maximum interaction force for a uniform temperature increment.

results will be used where required as a function of T_a in what follows.

3.4. Discussion

3.4.1. Displacements

Fig. 4 shows that, for high values of the elastic slenderness and uniform temperature change, longitudinal displacements are virtually zero except in the end portions of each tube sector. We adopt the term *breathing length* here, widely used by railway engineers for designating the end length of each (rail) sector where displacement accumulates. Correspondingly, Fig. 6 displays the end displacement as a function of λ_k. It is apparent that, by increasing the slenderness, the maximum displacement can be theoretically reduced below any desired value. More specifically, the graph shows that for $\lambda_k > 10$ the following approximation is valid:

$$\log_{10}\left(\frac{u_u(L)}{\alpha T_u L}\right) \approx -\log_{10}(\lambda_k) \Rightarrow L\sqrt{\frac{k}{EA}} \approx \frac{\alpha T_u L}{u_u(L)} \tag{10}$$

where $u_u(L)$ is the magnitude of the displacement caused by T_u at both ends of the tube.

For uniform temperature gradients along the tube, it can be shown that an equivalent approximation (using u_a and T_a instead of u_u and T_u) is valid as well if $\lambda_k > 10$. Accordingly, the combined end displacement $u(L) = u_u(L) + u_a(L)$ can be approximated as follows:

$$L\sqrt{\frac{k}{EA}} \approx \left(1 + \frac{T_a}{T_u}\right)\frac{\alpha T_u L}{u(L)} \tag{11}$$

It will be shown later that for representative values of the parameters, $\lambda_k > 10$ is verified; hence, the approximation in Eq. (11) is valid with generality (the relative error in the evaluation of $u(L)/(\alpha T_u L)$ as a function of λ_k is less than 4.1×10^{-9}). Therefore, if the end displacement is limited to $u(L) \leqslant u_{adm}$, then the elastic restraint required to satisfy such limitation is independent of the length of the tube, and its value is

$$k \geqslant EA\left(\frac{\alpha(T_u + T_a)}{u_{adm}}\right)^2 \tag{12}$$

3.4.2. Interaction forces

Fig. 7 shows the absolute value of the maximum normalised interaction force $f_u(L)$ at the end of the breathing length for uniform temperature changes. The relation tends to unity for the higher values of λ_k. This can be also proved to be true for linear temperature gradients.

$$\frac{|f_u(L)|\,L}{EA\,\alpha T_u} \approx \lambda_k \tag{13}$$

Thus, addition of both effects results in

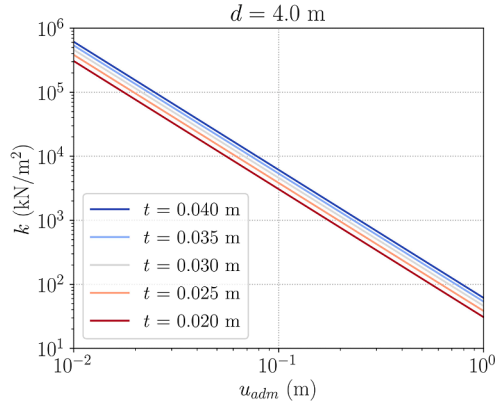

Fig. 8. Minimum required stiffness of the interface compatible with given admissible displacements for $d = 4.0$ m and different values of the tube thickness. S460 grade steel, $T_u + T_a = 60\,^{\circ}C$.

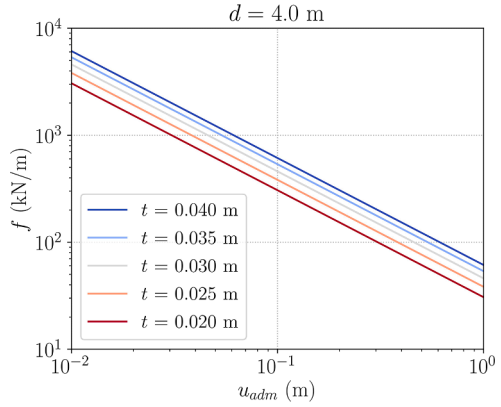

Fig. 9. Minimum required force along the interface compatible with given admissible displacements for $d = 4.0$ m and different values of the tube thickness. S460 grade steel, $T_u + T_a = 60\,^{\circ}C$.

$$\left|f(L)\right| \approx \frac{EA\,\alpha(T_u + T_a)}{L}\lambda_k = \alpha(T_u + T_a)\sqrt{EA\,k} \tag{14}$$

Consequently, if a limited maximum value of the interaction force is to be established in design $|f(L)| < f_{adm}$, the stiffness per unit length has to verify the following inequality:

$$k \leqslant \frac{1}{EA}\left(\frac{f_{adm}}{\alpha(T_u + T_a)}\right)^2 \tag{15}$$

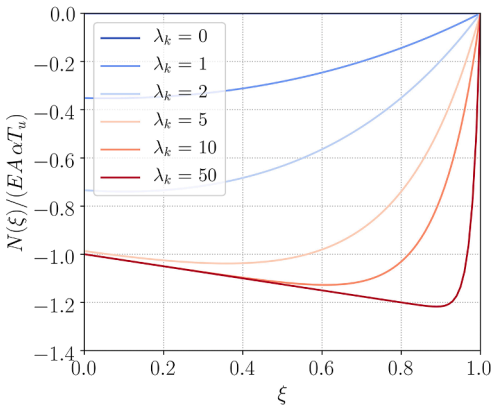

Fig. 10. Axial force caused by simultaneous action of uniform temperature and linear temperature gradient. $T_a/T_u = 0.25$.

3.4.3. Allowable range of stiffness values for the interface

The preceding limitations derived from the maximum allowable displacements and interaction forces restrict the interval of stiffness per unit length as follows:

$$EA\left(\frac{\alpha(T_u+T_a)}{u_{adm}}\right)^2 \leqslant k \leqslant \frac{1}{EA}\left(\frac{f_{adm}}{\alpha(T_u+T_a)}\right)^2 \tag{16}$$

The first inequality is represented in Fig. 8. It shows the minimum required stiffness per unit length of the support that is compatible with given admissible displacements of the end of a line section. On the other hand, the second inequality provides the minimum force per unit length that must be resisted along the interface, and is represented in Fig. 9. In both figures, $T_u + T_a = 60\ ^\circ$C has been chosen. While Eurocode 1 [17] (and equivalent codes) take into account uniform temperature increments and vertical/horizontal temperature gradients, no specification is given for temperature gradients along long sections of a linear infrastructure. Lacking specific data, the value of 60 ° C for the sum of both effects is a reasonable choice (see also Section 6.4). Figs. 8 and 9 provide preliminary design data to check the stiffness and strength requirements of R-Configuration viaduct piers and foundations for various tube cross-sections.

Regarding the magnitude of temperature variations, it can be anticipated that smaller local temperature changes, restricted to maximum lengths of some tens of kilometers, could be also expected in the HL infrastructure. This would imply some specific concerns related to axial expansion, particularly in R-Configuration. Therefore, a precise evaluation of local temperature gradients should be tackled in future refined analyses, including the possibility of both temperature drop into fog patches, as well as steep gradients between coastal areas of mild climate and inner areas of continental climate. The latter situation can be found, for example, near the coast of some Mediterranean countries during certain seasons of the year. Therefore, for detailed checks at design stage, the tube, piers and joints in R-Configuration should be analysed to consider those smaller local gradients.

3.4.4. Axial forces

It is also of interest to analyse typical values of axial force in the tube. Fig. 10 represents the axial force caused by simultaneous action of a uniform temperature and a temperature gradient, corresponding to ratio $T_a/T_u = 0.25$. It can be observed that, for high values of the slenderness, the axial force is enclosed in the interval $EA\alpha T_u \leqslant |N(\xi)| \leqslant EA\alpha(T_u + T_a)$. Moreover, for slenderness values below 5, axial forces markedly fall below the values corresponding to T_u for a fully-restrained tube, and tend to zero for very low λ_k. However, in a long structure with restrained longitudinal displacements, we show in the next section that the slenderness is above 10 and therefore, it is safe to choose $|N| = EA\alpha(T_u + T_a)$ for the design of the tube.

3.4.5. Representative values of the parameters

In order to understand the order of magnitude of the elastic constant k (interface stiffness), the expected displacements at the end of the line, the required ground strength and the elastic slenderness, we have included in Appendix B a study of a typical (notional) reinforced concrete pier-foundation system on medium-compact clay for a HL viaduct in R-Configuration with average span width $l = 30$ m.

Considering average soil properties for the clay, the study provides a stiffness of the pier-pile cluster system of 62240 kN/m in the longitudinal direction for the assumed geometry of the foundation. Then, for an average span of 30 m, the interface stiffness per unit length for this case is $k \approx 2075$ kN/m^2. Fig. 8 shows that with this interface stiffness value, the pier-foundation system should allow a maximum longitudinal end displacement of about 0.15 m. It would only take place in the last piers of the breathing lengths and would need specific engineering solutions to be accommodated. All piers in the largest, central part of each sector would experience almost no displacement according to Fig. 4.

B also includes the estimate of the horizontal failure load of the pile cluster, which is 9331 kN for the assumed data. Hence, considering again that the pier separation is 30 m in average, the ultimate force per unit length for the interface is 311 kN/m. Fig. 9 shows that the minimum required interface force to be resisted at the end of the breathing length for the estimated displacement (0.15 m) is about 300 kN/m.

Therefore, in this example there would be no security margin for the horizontal resistance of the foundation. This situation would need to be improved by increasing the foundation stiffness in the longitudinal direction, for example with inclined piles or ground anchors. Therefore, ground strength and deformability along the *breathing length* will be key design conditions for R-Configuration (expansion-restrained) viaducts.

Finally, we provide the order of magnitude of the elastic slenderness. Considering a Duplex steel tube with diameter $d = 4$ m and thickness $t = 25$ mm, the axial rigidity will be $EA = 62.832 \times 10^6$ kN. For the interface stiffness $k = 2075$ kN/m^2 of this example, the slenderness (6) is $\lambda_k = 0.00575L$. It will be larger than 10 when $L \geqslant 1.74$ km. This shows that long continuous infrastructures will always have values of slenderness larger than 10.

4. Control of tube shell stability

In addition to compressive thermal stresses —especially in R-Configuration because of the axial restraint—, a potential instability of the tube due to the inner vacuum is one of the main issues governing the structural design. The vacuum acting on the tube is represented as a net pressure of 101 kN/m^2 directed to the tube axis; it corresponds to the approximate value of Earth's atmospheric pressure at sea level. It is likely that internal elements such as the levitation/guiding rails will influence the stability analysis—most likely in a favourable manner because some kind of welded *ribs* may be expected at the inner, bottom part of the tube. The influence of such elements is neglected at the present stage of the analysis, given the lack of knowledge of structural details. Therefore, the bare tube is analysed with and without external ring stiffeners, as discussed in Section 2.

All analyses related to shell models described in Sections 4, 5, 6, 7 are based on an elastic shell consisting of a cylinder of constant diameter d and small, uniform thickness t. Those analysis are based on either (a) closed-form expressions obtained from thin shell theory, or (b) experimental tests, as it will be described in each corresponding section below.

4.1. Ideal critical pressure

In the first place, we evaluate the ideal (perfect geometry) critical load in a cylindrical shell due to combined longitudinal and radial compression. According to Brush and Almroth [18, Eq. (5.65)], the

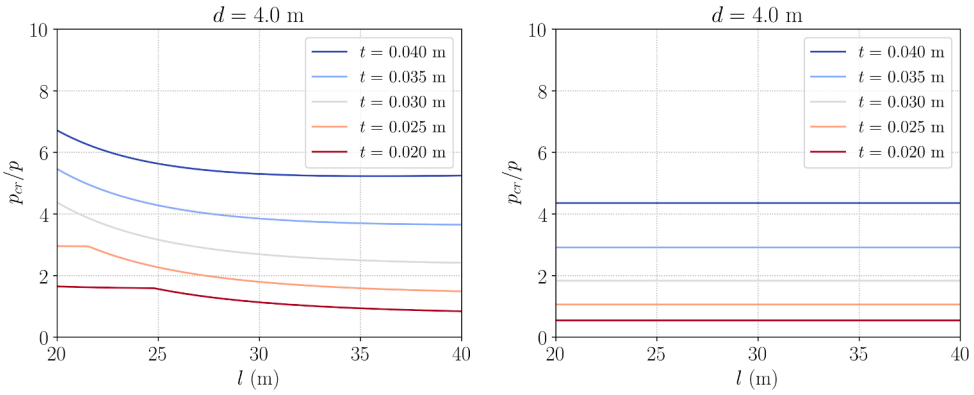

Fig. 11. Relative critical pressure for a S460 ($E = 200$ GPa) tube subject to internal vacuum with longitudinal stresses due to a 60°C temperature increment (left), and without longitudinal stresses (right, from Eq. (19)). $p = 101$ kPa. Simple support conditions at end edges.

critical uniform radial pressure in a cylinder of length l, simply supported along both edges, is determined by the mechanical and geometrical properties as follows:

$$p_{cr} = \frac{(\overline{m}^2 + n^2)^4 D/a^3 + \overline{m}^4(1-\nu^2)C/a}{(\overline{m}^2 + n^2)^2(n^2 + R\overline{m}^2)} \tag{17}$$

where $a = d/2$ is the cylinder radius; C and D are the shell membrane and bending stiffness, respectively: $C = Et/(1-\nu^2)$, $D = Et^3/(12(1-\nu^2))$; m is the number of semi-waves in the longitudinal direction; $\overline{m} = m\pi a/l$; n is the number of full waves in the radial direction corresponding to each buckling mode, and R is the ratio between axial and circumferential membrane forces. In the following subsections, critical pressures corresponding to both R-Configuration and F-Configuration are evaluated.

4.1.1. R-Configuration: restrained axial expansion

Thermal contraction of the tube will not lead to instability phenomena. Regarding thermal expansion, Eq. (17) can be used in R-Configuration if one admits that the ring stiffeners at support sections fully restrain radial displacements of the tube. In this case l is the span length and the assumption of simple support boundary conditions at the stiffeners is on the safe side. The ratio between the axial and circumferential membrane forces is

$$R = \frac{N_x}{N_\theta} = \frac{E\alpha(T_u + T_a)}{|p|}\frac{t}{a} \tag{18}$$

For Duplex steel, $T_u + T_a = 60\,°C$ and $p = -101$kPa, one obtains $R = 1544.55\,\frac{t}{a}$. The critical pressure can be obtained by trial and error for each ensemble of geometrical parameters. If the tube is stiffened by rings only at the supports, critical pressures are depicted in Fig. 11 (left). It can be seen that the margin of security is clearly insufficient for the smaller values of thickness.

4.1.2. F-Configuration: Free axial expansion

In this case $N_x = 0$ and thus $R = 0$. Eq. (17) would provide the critical pressures corresponding to the (axially unrestrained) tube with inner vacuum, but considering that it is stiffened at the supports (l is equal to the span length). If Eq. (17) is applied in such conditions of zero axial compression, it can be shown that the critical pressures increase, as it could be expected. However, this situation may probably be unrealistic, given that the magnitude of the longitudinal movements would render the placement of external ring stiffeners infeasible. Moreover, if the tube were to slide several meters or tens of meters, the optimal placement of some kind of *internal stiffening* for absorbing the local effects of vertical reactions at the piers should be analysed in detail for each span, and is outside the scope of the paper.

As a reference, the ideal buckling pressure in the case of an *infinitely long, non-stiffened tube*, with no axial force can be obtained from the Lévy's expression [18, Eq. (4.29)]:

$$p_{cr} = 3D/a^3 \tag{19}$$

which leads to the values in Fig. 11 (right).

The results in Fig. 11 underline the importance of the internal vacuum in the design. If, instead of almost-total vacuum, the internal pressure were about 25 kPa, as proposed by *Angels Capital* (one of the funders of Zeleros) [19], then the (ideal) relative critical pressures can be obtained multiplying the previous results by $101/(101-25) \approx 1.33$; it is apparent that the resulting values will be still too low to be safe, especially for the thinner walls. Nevertheless, the results presented so far correspond to an ideal situation where imperfections in the tube have

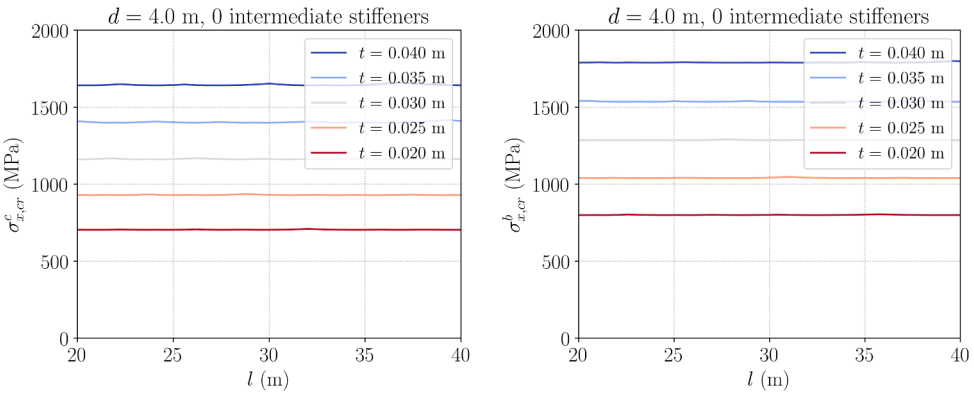

Fig. 12. Critical normal stress for a $d = 4$ m tube of S460 steel ($E = 200$ GPa) under axial compression (left) and bending (right).

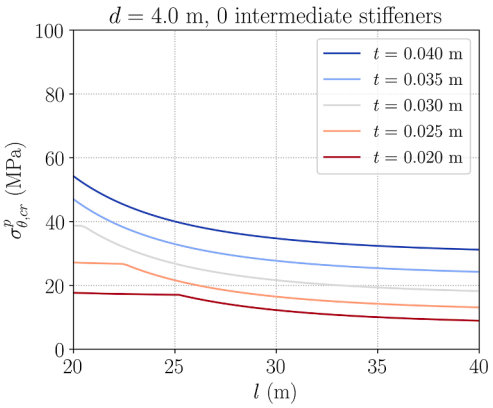

Fig. 13. Critical hoop stress for a tube of S460 steel ($E = 200$ GPa) under radial compression (ring stiffeners only at the supports).

not been considered. This aspect is dealt with in the next sub-section.

4.2. NASA SP-8007 design criteria for cylindrical shells

In 1968 NASA published reference [20], which provides values of critical forces in cylinders subjected to axial compression, radial compression, bending and torsion, and include correction factors for the theoretical formulas that were calibrated from laboratory tests. They also provide criteria for taking into account the interaction between the different internal forces. We summarize the formulas to determine critical longitudinal and hoop stresses in the tube for longitudinal compression, bending and external radial pressure, with minor changes in the notation. (For details and expressions of the factors in the formula, please refer to the original NASA publication):

$$\sigma_{x,cr} = \eta k_x \frac{\pi^2 D}{l^2 t} \text{(due to longitudinal compression and bending)} \tag{20a}$$

$$\sigma_{\theta,cr} = \eta k_\theta \frac{\pi^2 D}{l^2 t} \text{(due to external radial pressure)} \tag{20b}$$

Here, η is the plasticity factor, which we take equal to 1 in all cases; D is the shell bending stiffness; l is the length between ring stiffeners; t is the tube thickness, and k_x, k_θ are factors depending on: the number of longitudinal half-waves and transverse waves; Batdorf's Z tube curvature parameter; and a correction factor γ wihich is different in each three cases. The NASA expressions can be applied to a HL tube considering a cylinder length l equal to the typical viaduct span length, provided that stiffening rings are arranged at the support sections.

In the range of values of this study, the critical stresses provided by the formulas for axial compression, as well as for bending, are way above the yield stress —see Fig. 12. In contrast, for a tube under external radial compression and no longitudinal compression (with stiffeners only at the supports) the critical hoop stresses are much lower that the yield stress —see Fig. 13. The values obtained in this section serve as a reference in order to derive the design limit values for combined loadings, as it will be shown next.

5. Design loads and combinations

5.1. Characteristic values of loads

The values considered for the different load hypotheses are explained in the following. **Self weight** is idealised as a generalised load acting on the beam model: $g_{1,k} = \gamma_s A = \gamma_s \pi d t$. **Dead load** is also a generalised load acting on the beam model. We admit that its value is a fraction of the self weight, associated to the guiding and levitation systems, auxiliary conductions and equipment: $g_{2,k} = \beta g_{1,k}$ with $\beta = 0.5$. **Internal**

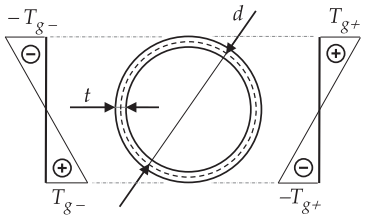

Fig. 14. Vertical temperature gradients acting on the cross-section of the tube: cooling of the upper face (left), heating of the upper face (right).

vacuum is an action that will produce effects on the shell model, but not in the beam model: p_k ($= -101$ kN/m^2). **Vehicle load:** At this stage it is analysed as a single point load acting on the beam model: ηF_k, where η is the *impact factor* and $F_k = 100$kN. The impact factor is the ratio between maximum dynamic and static effects due to the moving vehicle load exclusively (a precise definition is given in Section 9), and is also known in bridge dynamics as *impact coefficient* or *dynamic amplification factor* (DAF). As a reference value, the weight of the *Quintero One* vehicle is 50 kN [21]. In Sections 8 and 9, increased values of the vehicle weight will be discussed. **Wind load** is idealised as a generalised load acting on the beam model. In a first approach we take into account only the vertical wind effect acting downwards or upwards. We consider a vertical wind force coefficient $c_{f,z} = 0.9$ so that $w_k = c_{f,z} q_p d$, where q_p is the *peak velocity pressure* according to EN 1991–1-4 [22].

Temperature: Three different thermal variations are considered: (1) Uniform increase T_u measured from a reference temperature; (2) linear longitudinal gradient from $-T_a$ in one tube end to $+T_a$ in the opposite end; (3) linear vertical gradient of either T_{g+}/d (heating of the upper face) or T_{g-}/d (cooling of the upper face). According to Section 3, the combined effect of the first two thermal loads is bounded by $\epsilon_{k,T} = \alpha(T_u + T_a)$. The third thermal load implies prescribed curvatures: $\chi_{k,T} = -\alpha T_{g^+}/d$, $\chi_{k,T} = \alpha T_{g^-}/d$. Fig. 14 illustrates both temperature gradients acting on the tube.

The values of the uniform temperature increase and linear longitudinal gradient are explained in Section 3.4, while the vertical gradients are defined according to EN-1991–1-5 [17, Art. 6.1.4.1]. It should be noted that Eurocode EN-1991–1-5 [17, Art. 6.1.4.4] prescribes the consideration of thermal differences along the thickness in the design of large concrete box girder bridges, where significant temperature differences can occur between the inner and outer web walls of such structures. Conversely, since this effect is not established by EN-1991–1-5 as a design scenario for box steel girders, the through-thickness temperature gradient will not be considered in the analyses below.

5.2. Load combinations

We consider the load combinations according to [23, Annex A2: Application for Bridges (normative)].

1. Vehicle load is predominant

$$\gamma_{G,g} G_{k,g} + \gamma_{G,p} G_{k,p} + \gamma_{Q,F} Q_{k,F} + \gamma_{Q,w} \psi_{0,w} Q_{k,w} + \gamma_{Q,T} \psi_{0,T} Q_{k,T} \tag{21}$$

2. Thermal load is predominant

$$\gamma_{G,g} G_{k,g} + \gamma_{G,p} G_{k,p} + \gamma_{Q,T} Q_{k,T} + \gamma_{Q,w} \psi_{0,w} Q_{k,w} + \gamma_{Q,F} \psi_{0,F} Q_{k,F} \tag{22}$$

with the following combination and safety coefficients: $\gamma_{G,i} = 1.35$ (favourable); $\gamma_{G,i} = 1.00$ (unfavourable); $\gamma_{Q,i} = 1.50$; $\psi_{0,F} = 0.8$; $\psi_{0,w} = 0.6$; $\psi_{0,T} = 0.6$. Wind load will be shown to be small and its effects need not be considered predominant. Vacuum has been consid-

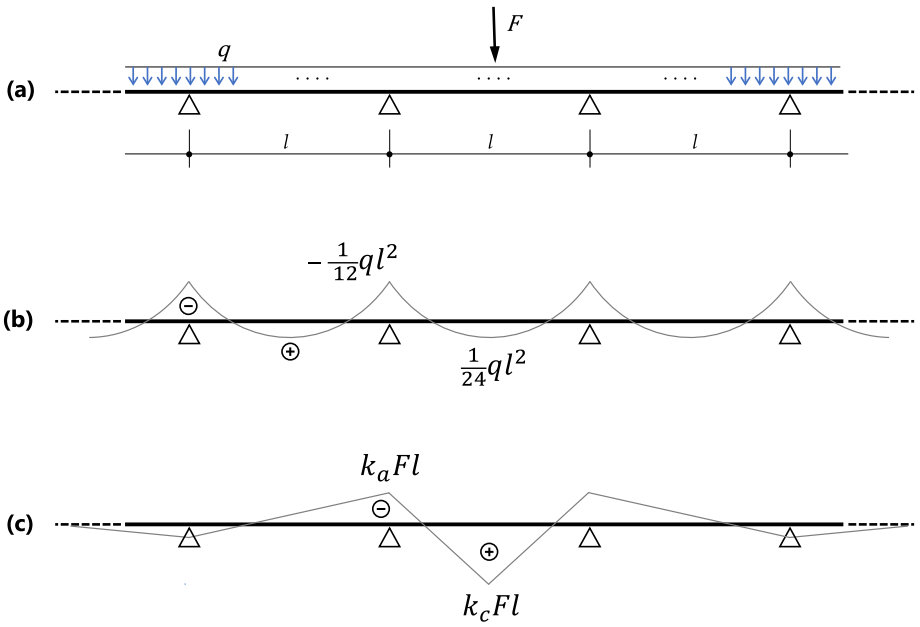

Fig. 15. Structural system for a R-Configuration viaduct: (a) System with loads; (b) Bending moments due to a uniform load q; (c) Bending moments due to a point load F acting at the mid-span section. Bending moments are valid for both R-Configuration and F-Configuration.

ered as a permanent action. In case it is considered a variable action that can vanish during maintenance, it has been verified that the margins of safety are not lower than when considered permanent.

6. Evaluation of stresses

As explained in Section 2, characteristic values of stresses result from the sum of bending and axial stresses evaluated with a beam model, plus the stresses corresponding to local effects—due to the internal vacuum— evaluated with a shell model. The loads mentioned in Section 5 that result in bending of the tube will produce equal traction and compression stresses in the upper and lower fibres (UFb, LFb) of the tube. Therefore, in R-Configuration (restrained axial expansion), maximum *total* longitudinal stresses will occur either in the UFb or LFb as a result of longitudinal thermal stresses in severely hot or cold days of the year.

Permanent loads create traction in the LFb at mid span, as well as in the UFb at the supports, and compression in the opposite fibres. Conversely, vehicle load, wind and vertical temperature gradient T_{g^+}/T_{g^-} can alternate signs. Wind effects are considered identical in upward and downward directions. It will be shown that wind action is small compared to other effects, and therefore, wind in the horizontal direction is not considered. In principle, a maximum impact effect (η) of the vehicle[2] could be expected if the critical (resonance) speed of the first bending mode were reached, which would result in similar upwards and downwards displacements due to the periodicity of the structure and low structural damping. In such case, very high impact factors could occur for typical damping values in steel, bridge-like structures: *cfr.* 0.5% from [24] *vs.* 5.0% from [10]. This hypothesis will be revised in depth in Section 9.

The worst scenario is to be expected when the vehicle loads, wind loads and temperature gradients T_{g^+}, T_{g^-} create stresses of the same sign as the permanent loads, resulting in identical tractions and compressions in the UFb and LFb. Additionally, the axial forces $N = EA\alpha(T_u + T_a)$ would be added, leading to maximum traction during winter and maximum compression in summer.

Because maximum expected tractions and compressions would be almost identical in magnitude, only compressions will be considered hereinafter —which allows to deal also with the required stability assessment. Consequently, the locations to compute longitudinal stress values in the ULS verification related to the tube strength are the LFb at the supports (referred to as "Combination I" in what follows) and UFb at mid span ("Combination II"). Such values will be analysed subsequently in conjunction with hoop stresses.

6.1. Section forces in the beam model

We compute the internal forces associated to longitudinal normal stresses using a beam model on simple supports with an infinite number of spans (see Fig. 15). This model is used for all transverse loads, as well as for the thermal vertical gradient. As transverse loads do not cause axial forces in this model, there is no need to consider horizontal springs in the case of the R-Configuration, and bending moments/shear forces evaluated with it are valid for both configurations (restricted and free axial expansion). Bending moments due to uniformly distributed loads are identical in each span of length l. The vehicle point load is placed at the centre of one of the spans. On the other hand, for the R-Configuration, thermal axial forces have been evaluated according to Section 3.4.4 using the model explained therein.

Notice that bending moments caused by uniformly distributed loads have equal values for both Bernoulli–Euler and Timoshenko beam models, whereas bending moments caused by the vehicle depend on the shear coefficient $12EI/GA_sl^2$. For thin-walled ring cross-sections, the shear area is $A_s = 0.5A$ and the shear coefficient is independent of the

Table 2
Characteristic values of the forces at the support sections: downward wind, vehicle force and cooling of the upper face of the tube (Combination I).

Type	Action	N_{Ek}	$M_{z,Ek}$
$G_{k,g}$	permanent	0	$-\frac{1}{12}g_k l^2$
$Q_{k,F}$	vehicle	0	$\eta k_a F_k l$
$Q_{k,w}$	wind	0	$-\frac{1}{12}w_k l^2$
$Q_{k,T}$	temperature	$-EA\alpha(T_u + T_a)$	$-\frac{1}{2}EW_{el,z}\alpha T_{g^-}$

[2] Not to be confused with the plasticity factor in Section 4.

Table 3
Characteristic values of the forces at mid-span sections: downward wind, vehicle force and heating of the upper face of the tube (Combination II).

Type	Action	N_{Ek}	$M_{z,Ek}$
$G_{k,g}$	permanent	0	$\frac{1}{24} g_k l^2$
$Q_{k,F}$	vehicle	0	$\eta k_c F_k l$
$Q_{k,w}$	wind	0	$\frac{1}{24} w_k l^2$
$Q_{k,T}$	temperature	$-EA\alpha(T_u + T_a)$	$\frac{1}{2} EW_{el,z}\alpha T_{g^+}$

section wall thickness. The bending moment at the midspan section and at the adjacent support section are, respectively, $M_{z,c} = k_c Fl$, $M_{z,a} = k_a Fl$, where $k_a < 0$; the approximate values of the coefficients for $l \in [20\text{ m}, 40\text{ m}]$ are given by the following fitting formulae:

$$k_c = 6.50675 \times 10^{-6}\ l^2 - 5.35926 \times 10^{-4}\, l + 1.82874 \times 10^{-1} \tag{23a}$$

$$k_a = 6.50675 \times 10^{-6}\, l^2 - 5.35926 \times 10^{-4}\, l - 6.71259 \times 10^{-2} \tag{23b}$$

Tables 2 and 3 gather the characteristic values of the relevant section forces for the support and mid-span sections in Combinations I and II as defined above.

6.2. Stresses in the shell model

Stresses due to vacuum in the vicinity of stiffening rings can be computed with a shell model. Vacuum is equivalent to a pressure that points to the tube axis, and produces normal hoop stresses that are given by the simple formula for a ring (25). Besides, ring stiffeners restrain the radial displacements and induce additional stresses; these can be estimated assuming that the stiffeners are very rigid and its deformability can be neglected. Longitudinal and hoop stresses due to vacuum pressure p_k at sections with ring stiffeners result from shell bending moments M_{xx} and $M_{\theta\theta}$ and are given by the following expressions that can be deduced from [25, Table 13.2, n. 15]:

$$\sigma^p_{x,k} = \pm\frac{1}{2}\sqrt{\frac{3}{1-\nu^2}}\,\frac{d}{t}\,p_k, \quad \sigma^p_{\theta,k} = \pm\frac{1}{2}\sqrt{\frac{3\nu^2}{1-\nu^2}}\,\frac{d}{t}\,p_k \tag{24}$$

Longitudinal stresses decay exponentially with the distance to the supports. Thus at mid-span one has:

$$\sigma^p_{x,k} = 0, \quad \sigma^p_{\theta,k} = \frac{1}{2}\,\frac{d}{t}\,p_k \tag{25}$$

Uniform temperature changes would also cause stresses in the vicinity of ring stiffeners if the material of the stiffener were different from the material of the tube, due to differential dilatation. At this stage of the analysis we consider that ring stiffeners at supports are made of steel; therefore, we disregard local stresses due to temperature changes.

6.3. Characteristic stress values

The characteristic values of stress for each action are evaluated by superposition of the results from the beam and shell models in Combinations I and II.

6.4. Case study

In this section the contribution and order of magnitude of each action is illustrated by means of an example of HL structure with restrained expansion (R-Configuration). The structural model is represented in Fig. 15. The geometric data are: $l = 28$ m; $d = 4.0$ m; $t = 0.025$ m. From these values,

Table 4
Characteristic values (MPa) of longitudinal stresses in R-Configuration (restrained axial expansion) at support and mid-span sections, for 4.0 m diameter, 0.025 m thickness and 28 m span. Impact factor η defined in Sections 5.1 and 9.

Type	Action	$\sigma_{x,Ek}(x = 0, y = -2.0\text{m})$ Combination I	$\sigma_{x,Ek}(x = +14.0\text{m}, y = +2.0\text{m})$ Combination II
$G_{k,g}$	permanent	−7.64	−3.82
$G_{k,p}$	vacuum	−14.67	0
$Q_{k,F}$	vehicle	-0.69η	-1.54η
$Q_{k,w}$	wind	−0.86	−0.43
$Q_{k,T}$	temperature	-171.21 ∓ 65.36	−172.38

Table 5
Characteristic values (MPa) of hoop stresses at support and mid-span sections, for 4.0 m diameter, 0.025 m thickness and 28 m span. Valid for both R-Configuration (restrained axial expansion) and F-Configuration (free axial expansion).

Type	Action	$\sigma_{\theta,Ek}(x = 0, y = \pm 2.0\text{m})$	$\sigma_{\theta,Ek}(x = 14.0\text{m}, y = \pm 2.0\text{m})$
$G_{k,p}$	vacuum	4.40	−8.08
$Q_{k,T}$	temperature	36.00 ∓ 19.61	0

Table 6
Design values (MPa) of longitudinal stresses in R-Configuration (restrained axial expansion) at support (left) and mid-span (rigth) sections, for 4.0m diameter, 0.025m thickness and 28m span. Impact factor η defined in Sections 5.1 and 9.

	$y = -2.0\text{m}$		$y = +2.0\text{m}$	
	Combination I		Combination II	
Action	$\gamma(\cdot\psi)$	$\sigma_{x,Ek}$	$\gamma(\cdot\psi)$	$\sigma_{x,Ek}$
G_g	1.35	−7.64	1.35	−3.82
G_p	1.35	−14.67		0
Q_F	1.20	-0.69η	1.20	-1.54η
Q_w	0.90	−0.86	0.90	−0.43
Q_T	1.50	−171.21	1.50	−172.38
	$\sigma_{x,d} =$	$-287.71 - 0.82\eta$	$\sigma_{x,d} =$	$-264.12 - 1.85\eta$

section properties are: $A = 0.314159\text{ m}^2$; $W_{el,z} = 0.314159\text{ m}^3$. The self-weight forces for the beam model and the inner vacuum pressure are: $g_{1,k} = 24.50\text{kN/m}$; $g_{2,k} = 12.25\text{ kN/m}$; $p_k = -101\text{ kN/m}^2$. We consider a vehicle of weight $F_k = 10 \times 10^3\text{kg}\cdot 9.81\text{ m.s}^{-2} \approx 100$ kN. For now, we do not specify the impact coefficient η. For a peak wind pressure $q_p = 1.148\text{ kN/m}^2$ and a vertical force coefficient $c_{f,z} = 0.9$ one obtains the generalised force $w_k = 0.9\cdot 4.0\text{ m}\cdot 1.15\text{ kN/m}^2 = 4.13\text{ kN/m}$. The thermal action is strongly dependent on the geographical location of the line. The following values have been adopted: $T_u + T_a = 60°\text{C}$; $T_{g^+} = 0.7\cdot 18°\text{C} = 12.6°\text{C}$; $T_{g^-} = 0.9\cdot 13°\text{C} = 11.7°\text{C}$. Here, the value for the uniform temperature increase can be representative for South-western Europe and need be considered as an order of magnitude rather than as a precise design value. As mentioned before, the longitudinal gradient along the tube is not considered in the standards; however, even for very long lines, the semi-differences in the maximum values of the temperature at line ends found in national temperature maps are around 5°C; rather small compared to the temperature increase. The vertical gradient corresponds to an unsurfaced steel structure [17, Art. 6.1.4.1]. For the sake of simplicity and on the safe side, a simultaneity factor $\omega_M = 1.0$ for the joint action of the uniform and

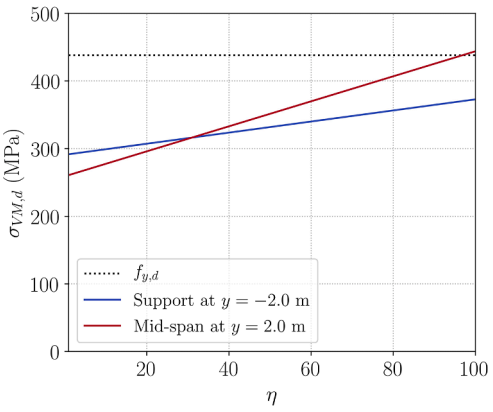

Fig. 16. Von Mises design stresses for the case study structure ($l = 28$ m, $d = 4.0$ m, $t = 0.025$ m).

the gradient components (see [17, Art. 6.1.5]) has been adopted.

6.4.1. *Characteristic values of stresses*

The longitudinal and hoop stresses in the UFb and LFb at the support and mid-span sections are summarised in Tables 4 and 5 for each action. Both for the support and mid-span sections, it can be observed that the thermal stresses exceed by large the remaining effects. This conclusion is valid even for high values of the impact coefficient.

6.4.2. *Load combinations*

Table 6 summarises the design values of the longitudinal stresses in both relevant sections, corresponding to the case study presented in the preceding subsection. The safety and combination coefficients from Section 5.2 have been employed. Limitations arising from the tube stability are not taken into account for now. Temperature is considered to be the predominant action. This hypothesis is valid for impact coefficients as high as 249 at the LFb of the support sections, as well as for impact coefficients below 112 at the UFb of the mid-span sections.

On the other hand, the design values of the hoop stresses from the vacuum pressure are: $\sigma^{p}_{\theta,d} = 1.35{\cdot}4.40 = 5.94$ MPa (support); $\sigma^{p}_{\theta,d} = 1.35{\cdot}(-8.08) = -10.91$ MPa (midspan). The Von Mises stress at a given cross-section point is given by

$$\sigma_{VM,d} = \sqrt{\sigma^2_{x,d} + \sigma^2_{\theta,d} - \sigma_{x,d}\,\sigma_{\theta,d}} \tag{26}$$

This formula provides quasi-linear relations between the impact coefficient and the Von Mises design stress: Fig. 16 shows the results for the support and the mid-span sections. Remarkably, mid span cross-sections yield for lower impact factors than support cross-sections. It can be concluded that, except in the case of extremely strong dynamic effects, the importance of vehicle loads is relatively low compared to thermal loads when expansion is restrained (R-Configuration). However, it should be stressed that these results do not consider the potential buckling of the tube, which will introduce important limitations as shown in the next section.

7. Structural safety margins

Safety checking for combined stresses will be carried out for a representative set of cases with tube diameter $d = 4.0$ m, span lengths ranging between 20 m and 40 m and wall thicknesses ranging between 20 mm and 40 mm. The impact coefficient offers a simple, straightforward interpretation of the importance of the effect of the vehicle; therefore, its maximum allowable value will be used as an index of the safety margin. For given span and wall thickness the maximum allowable impact coefficient is determined as follows:

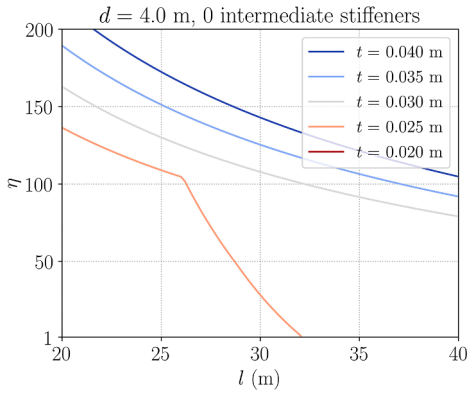

Fig. 17. Maximum allowable impact factor in a S460 steel tube with stiffeners only at the support sections in R-Configuration (restrained axial expansion). Actions described in Section 6.4.

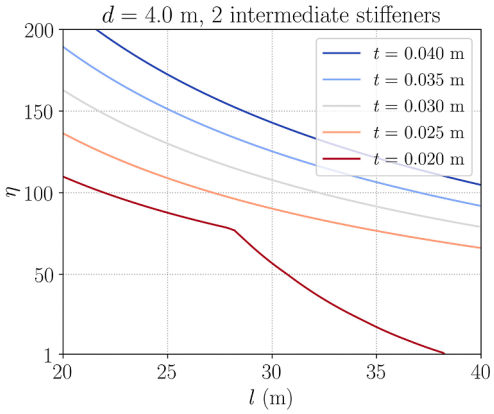

Fig. 18. Maximum allowable impact factor in a S460 steel tube with stiffeners at the support- and 2 intermediate sections in R-Configuration (restrained axial expansion). Actions described in Section 6.4.

1. Start from an impact coefficient $\eta = 1$. In general, this will be not exhaust the capacity of the structure in the cases analysed here.
2. Determine the structural capacity ratio for η in both *Combinations* (I or II) from the strength condition without consideration of buckling: $\sigma_{VM,d}/f_{y,d} \leqslant 1$, (Von-Mises stress is determined according to Section 6). Select the maximum ratio among the two values.
3. Determine the structural capacity ratio for η in Combinations I and II from the buckling control condition:

$$\frac{\sigma^{c}_{x,d}}{\sigma^{c}_{x,cr}} + \frac{\sigma^{b}_{x,d}}{\sigma^{b}_{x,cr}} + \frac{\sigma^{p}_{\theta,d}}{\sigma^{p}_{\theta,cr}} \leqslant 1 \tag{27}$$

   (Critical stresses of the tube under compressive, bending and radial loads are calculated according to Section 4. Stresses in the numerator in absolute value). Select the maximum ratio among the two values.
4. Retain the maximum of both capacity ratios from previous points 2 and 3. If it is lower than 1, repeat the calculation for an increased value of η. If it is larger than 1, stop and search for an exact value of η which leads capacity ratio equal to one within the last interval of checked values.

In the following subsections, maximum allowable impact factors are determined for both R-Configuration and F-Configuration.

7.1. *Results for restrained axial expansion (R-Configuration)*

Results for 4 m diameter tubes with ring stiffeners at support sections

Table 7
Critical hoop stresses (MPa), design hoop stresses (MPa) and structural capacity ratio for a non-stiffened $d = 4$ m S460 steel tube under radial compression in F-Configuration (free axial expansion).

t (mm)	40	35	30	25	20
$\sigma^p_{\theta,cr}$	19.780	15.144	11.126	7.727	4.945
$\sigma^p_{\theta,d}$	6.818	7.791	9.090	10.908	13.635
$\sigma^p_{\theta,d}/\sigma^p_{\theta,cr}$	0.3447	0.5145	0.8170	1.4117	2.7573

and no other intermediate stiffeners are shown in Fig. 17. A noticeable effect is the rapid loss of capacity (due to buckling) for the tube with thickness $t = 25$ mm when the span length is larger than 26 m. It is not possible to design 20 mm thick tubes with no intermediate stiffeners.

Fig. 18 shows that with two intermediate, equidistant ring stiffeners, the 4 m diameter tube instability due to vacuum is controlled even for long spans and low values of thickness.

It is worth mentioning that for this configuration, the ratio of mechanical capacity absorbed by the thermal action (assuming it is predominant and steel grade is S460) is very high: $\sigma^c_{x,d}/f_{y,d} = 1.5{\cdot}172.38/(460/1.05) = 0.59$. Therefore, in R-Configuration it is crucial to use S460 steel (or higher grades), as stresses due to thermal expansion can't be reduced increasing the cross-section area.

7.2. Results for free axial expansion (F-Configuration)

We admit that in a tube that is free to expand no ring stiffeners are used, as discussed in Section 2. Then, in agreement with the ideal value from Lévy's formula, Eq. (19), critical stresses tend to the following value [20, Eqs. (19) & (21)]: $\sigma_{\theta,cr} = \eta\gamma(3D)/(a^2t)$, with $\gamma = 0.9$ and $\eta \approx 1$.

The preceding expression of $\sigma_{\theta,cr}$ does not depend on the span, since we admit that no radial restraint exists along the whole tube. Hoop design stresses $\sigma_{\theta,d}$ are calculated according to Eq. (25) with a security factor $\gamma_d = 1.35$. The ratio of structural capacity consumed for the case of inner vaccum is given by $\sigma_{\theta,d}/\sigma_{\theta,cr}$. It is straightforward to check that, in this case, the permanent, vehicle and wind actions scarcely influence the structural capacity compared with the critical stress due to the internal vacuum. Results for $d = 4$ m are included in Table 7 and show that a minimum thickness of 30mm is required for this configuration.

Built-up tubes with less thickness and orthotropic stiffening could be more economical, but this analysis is out of the scope of this article. For this configuration, in which there is no restriction to thermal expansion, the use of lower grade steel (as S355) could be considered. However, as already mentioned, the problem of very large movements of the structure on the supports would require non-standard technological solutions.

8. Fatigue assessment

According to several sources (see for instance [26]), the frequency of travel of pods in a HL line may be of the order of minutes. Therefore, HL infrastructure designed for a service life of 100 years needs to be assessed against fatigue, at least in a first approach. The reference document in Europe for such assessment is EN1993-1–9 [27]. Section 6.4 illustrates that the stresses due to the vehicle weight are very small in comparison to other effects. Consequently, a suitable approach is to verify whether the stress ranges in the HL tubes are below the *cut-off limit* $\Delta\sigma_L$. In such case, no further fatigue assessment will be required. A first step to determine $\Delta\sigma_L$ is to choose a detail category in EN1993-1–9. This, in turn, involves the selection of the type/location of welded unions among the different parts of a typical HL tube.

For this purpose, we first make the assumption that transportation by road of stretches of several meters long is feasible. Such stretches, similar to *slices*, could be welded previously in plant (this option is demonstrated by some videos published by Hyperloop TT). While longitudinal seams would probably be located at the bottom generatrix, circumferential seams would be used for joining the slices. Depending on the particular construction method adopted, some of these circumferential seams could be located not far from mid-span. Therefore, for both R-Configuration as well as F-Configuration, it is on the safe side to evaluate the fatigue stress range by using the bending moment at mid span for the 10×10^3 kg·9.81 m.s$^{-2} \approx 100$ kN vehicle load: $M_{z,\mathrm{Fk}} = 0.1730 F_k l = 475.1$ kNm for span equal to 28 m. These welds would undergo normal stress ranges $\Delta\sigma_{E,2}$, corresponding to 2×10^6cycles and a detail category 71 in table 8.3 of EN1993-1–9, as long as the thickness is not higher than 25 mm.

On the safe side, we adopt the *safe life* assessment method mentioned in EN1993-1–9, which leads to a partial factor $\gamma_{\mathrm{Mf}} = 1.35$. According to EN1991-2 [24], we use partial factor $\gamma_{\mathrm{Ff}} = 1.00$. We take also a conservative approach by admitting that the stress range is twice the value of the stress; then, for a diameter of 4.0 m and the most unfavourable thickness of 20 mm, the following characteristic stress ranges are obtained (dynamic impact factor still not included): $\Delta\sigma(\gamma_{\mathrm{Ff}}F_k) = 3.78$ MPa. Finally, the damage equivalent factors for (road) bridges are taken from EN1993-2 [28], where a maximum (approximate) value $\lambda_{\max} = 2.0$ is specified for spans in the range of 20 to 40 m, at mid-span sections (smaller values for support sections). Therefore, one gets the following stress ranges (without impact factor): $\gamma_{\mathrm{Ff}}\ \Delta\sigma_{E,2} = 7.56$ MPa.

The cut-off limit for normal stresses in EN1993-1–9, for the category of detail involved is $\Delta\sigma_L = 28.7$ MPa. When this cut-off limits is reduced by $\gamma_{\mathrm{Mf}} = 1.35$, the impact factor η required for reaching $\Delta\sigma_L$ would be $\eta = 28.7\ \mathrm{MPa}/(1.35{\cdot}7.56\ \mathrm{MPa}) \simeq 2.8$. If the damage equivalent factors for railway bridges are used, then $\lambda_{\max} = 1.4$ and additional margin is available for dynamic effects. The margin also increases to $\eta = 3.5$ if the tube thickness is 25 mm, but of course it would reduce for vehicles heavier than 100 kN. However, in the next section it will be shown that the impact factors are low enough to discard the need of a more refined fatigue analysis at this stage.

If transportation by road of tube stretches were not feasible, an alternative option would be to build the tube from curved panels that could be transported inside the previously built tube length. Such panels could be suitably welded with overlap close to 1/5 of the span length, in order to minimise bending moment from the permanent loads. In such case, analogous analyses for the normal (and shear) stresses as the ones described before demonstrate that the allowable impact factor increases.

Finally, since diurnal temperature variations could raise some concerns related to fatigue arising from thermal loading, those effects will be briefly discussed. On average, for a continental climate with low air humidity, diurnal temperature variations can be estimated conservatively in $\Delta T = 20\ ^\circ C$, with a total number of cycles around 36500 (365 days/year times 100 years of service life). Therefore, the expected normal stresses will be around 1/3 of those for the maximum yearly event given in Table 6, which were obtained for a temperature increase of 60 °C. This would imply less than 60MPa in longitudinal direction. Based on fatigue strength curves on EN1993-1–9 [27] (Fig. 7.1, detail category 71), the minimum number of cycles that the tube will be able to withstand for this stress range is far more than the 36500 estimated in service, even after the application of the safety factors discussed previously in this section.

9. Dynamic response

In addition to the phenomena analysed in previous sections, the structure will also undergo dynamic effects produced by the pod travelling at Ultra-High-Speed (UHS), whose importance is hitherto uncertain due to lack of specific research in this area. However, the problem of vibration of continuous beams has been tackled extensively in the past (see [29–31] for instance), including some contributions from the authors [32].

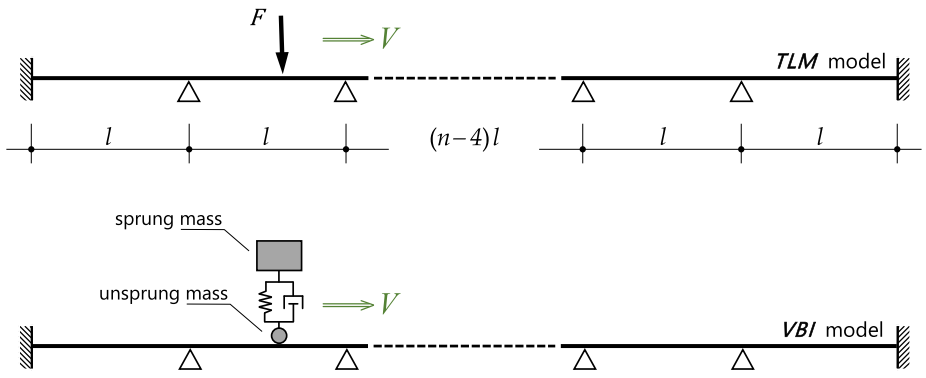

Fig. 19. Travelling load model (TLM) and vehicle-bridge interaction model (VBI) for viaducts of *n* spans.

Outcomes of the recent pioneering publication on UHS by Alexander and Kashani [10] envisage very high dynamic amplification factors (DAF) for HL systems. Even if the results in [10] are well supported by the analyses described in such paper, their work is partly based on empirical data that define fundamental frequencies typical for actual *railway bridges* (RWB). Although the formulation in [10] is of general nature and allows any viscous damping to be considered, a high damping ratio equal to 5% is employed in the main results plots (Figs. 4 to 7 in that article), while such level of damping is not usual in RWB of medium to long spans. For spans longer that 20m, Eurocode 1 [24] prescribes 1.0% damping for prestressed bridges and 0.5% damping for metallic/composite bridges. Regarding the natural frequencies, here it will be shown that the expected values are higher in HL structures than in RWB of the same spans, which has a strong influence in the predicted dynamic response.

A later work from Ahmadi, Alexander and Kashani [11] explores also the lateral vibrations of the HL tubes by using a simplified model that provides interesting insight. To reasonably limit the scope of this paper, such lateral effects will not be addressed here. However, it should be mentioned from the results in reference [11] that tube/pier stiffness ratios, damping ratios and lateral natural frequencies (in relation to the vehicle speed) could play a major role in the transverse resonant response, as well as the number of spans. The conclusions of the present paper will provide new information to foster future research of the lateral behaviour, once the essential dimensions of HL systems required to withstand the key external actions have been discussed here.

The large body of previous knowledge about vibrations of RWB under high-speed trains is a suitable departure point for the dynamic analysis of HL structures. Standards such as Eurocode EN1991–2 [24] and others typically deal with dynamic effects in ULS analysis of RWB by means of DAFs. A single definition of what a DAF represents does not exist in literature, but a convenient and conservative means of defining it for the analysis of continuous HL stretches is as follows:

$$\eta = \max\left\{\frac{\max\limits_{\forall t} S_{\mathrm{dyn}}(x,t)}{|S_{\mathrm{stat}}(x)|} : \forall x\right\} \tag{28}$$

In Eq. (28), variable x locates the section corresponding to an abscissa that experiences maximum static effect (*movement* or *internal force*) S_{stat} when one vehicle moves along the continuous beam, and maximum dynamic effect ($\max\limits_{\forall t} S_{\mathrm{dyn}}$) for the same vehicle. Self-weight, temperature, wind and other effects different from vehicle load are excluded from Eq. (28). Furthermore, the amplification can be evaluated both for positive and negative values of each effect, which is the strategy followed in this article. Retaining the maximum DAF among the various cross-sections is intentionally conservative at this stage for two reasons: first, the broad scope of the article, which necessarily requires to restrict the depth of the dynamic analysis; second, the limited relevance of the dynamic effects, as it will be shown below.

Moreover, in Section 6.4.6.5 of EN1991–2 [24] it is established that the DAF (dynamic enhancement or *impact coefficient*) be computed as the dynamic amplification φ'_{dyn} of the response, while such *response* is a term that is often associated to *displacement* response by RWB engineers (see for instance [33], with contributions from major European railway networks). Formula (6.15) in [24] is in line with such interpretation of φ'_{dyn} as a displacement-based impact coefficient, since a general interpretation for every type of structural response (including internal forces) would drive directly towards an amplification exclusively through the irregularity factor $\varphi''/2$, without an actual need to define φ'_{dyn}. In the background of such typical usage of φ'_{dyn} lies the fact that computing displacement impact coefficients is a relatively straightforward operation in dynamic analyses.

Therefore, in order to limit the scope of the study, Eq. (28) will be applied by taking maximum positive/negative displacements as explained above. The critical analysis of the displacement-based procedure deserves specific research to be dealt with in separate studies.

The HL case study selected in Section 6.4 has been also considered here. A viscous damping ratio of 0.5% is used, as for steel bridges in [24]. In lack of specific data, the radius of gyration of the dead loads in the tube, see Section 5, is assumed to be 80% of the radius: 1.6 m. In line with the R-Configuration (restrained axial expansion) from Section 2, the tube is fixed at both ends and simply supported at the intermediate piers. The fixed end boundary conditions are consistent with the significant axial restraint that is to be provided in R-Configuration viaducts —if not at every pier, at least at discrete "rigid" (more costly) piers which should leave a number of "weaker" (cheaper) piers between them. The sensitivity to the number of spans and boundary conditions will be discussed.

Results are based on a discretisation with 12 Timoshenko beam el-

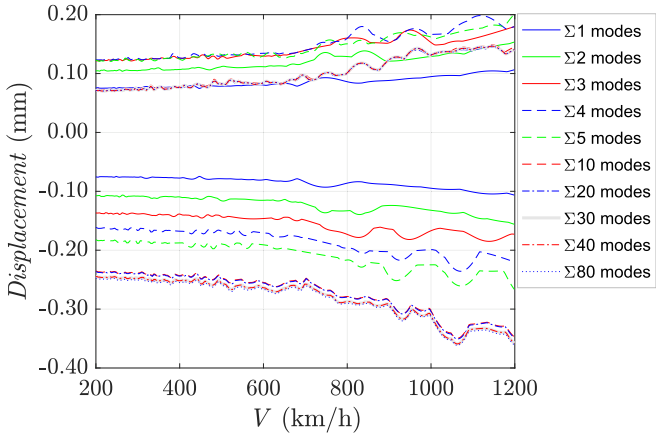

Fig. 20. Sensitivity of max./min. displacement to the number of modes for a ten-span viaduct.

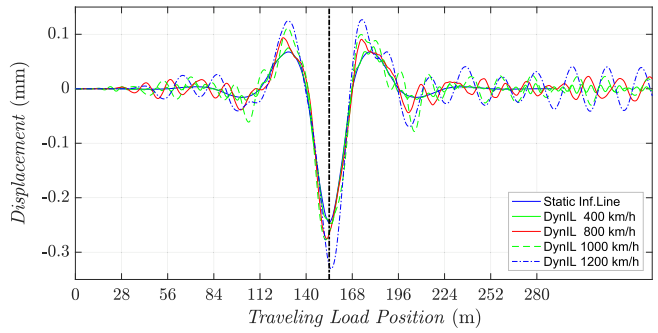

Fig. 21. Center of span #6. Static/dynamic influence lines for a 10 span tube (28 m per span, 3 clusters). Spans numbered starting from 1 at the leftmost span of the tube.

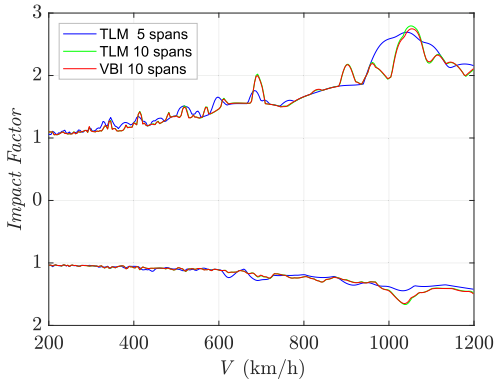

Fig. 22. Dynamic amplification factors computed with 3 clusters of modes.

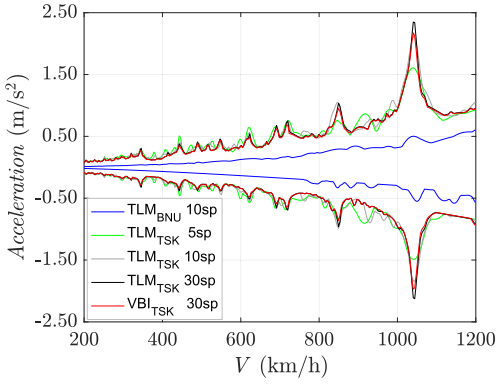

Fig. 23. Maximum accelerations in the tube for different numbers of spans, considering two clusters of modes (cut-off frequency ≈ 50 Hz).

ements per span and a pod travelling at a constant speed. A previous proprietary FORTRAN code has been adapted to run both the modal as well as the transient mode superposition analyses. All vibration modes are assigned 0.5% damping. Two different vehicle modelisations are compared, see Fig. 19: travelling load model (TLM) and vehicle-bridge interaction (VBI) model. For the TLM, the weight of the pod is a point force of 10×10^3 *kg*·9.81 m.s^{-2} ≈ 100 kN. In the VBI model, the vehicle is simplified to a mass-spring-dashpot system of sprung mass 9000 kg, with frequency of 1.0 Hz and damping ratio 20%. Such frequency and damping values are typical in modern railway vehicles ([34,35]) and are adopted in absence of reliable information from HL pod suspension systems —which are expected to vary among HL competitors. To complete a total mass of 10000 kg, an extra mass of 1000 kg is also considered in the VBI model, that takes into account an eventual *unsprung* weight of the levitation/guiding system; the unsprung mass has a vertical displacement identical to that of the HL tube at the section where the vehicle is instantaneously located. In lack of reliable data, no rail irregularities are considered at this stage of the study.

Figs. 20 and 21 represent the displacement of the tube. Mid-span and quarter-span sections of all spans have been considered in Figs. 20, 22 and 23. Since the adopted FEM solution is based on a modal approach, the influence of the number of modes considered for superposition is examined first. As it is known, natural frequencies occur in *clusters* for multi-span beams, where each cluster contains a number of "close" natural frequencies equal to the number of spans. Fig. 20 shows the sensitivity to the number of modes for a 10 spans viaduct: it is clear that at least the first complete cluster is necessary to obtain a good approximation, but a slight error remains in the predicted displacement —practically constant over the speed axis— which slowly decreases with the number of clusters considered. It can also be seen that positive displacements converge faster than negative ones.

No sharp resonance peak is observed in Fig. 20, even if it could indeed be expected for a periodic structure with low damping. It should be noticed that the critical speed of the fundamental mode is not reached at 1200 km/h. Such critical speed, for a lowest natural bending frequency of 11.82 Hz and span $L = 28m$ is $V_{crit} = \omega L/\pi = 2383$ km/h. In modern RWBs, a reference value of high fundamental frequency for such span length is 7.8 Hz [24], way below the lowest bending frequencies predicted for the HL tube. Table 8 gathers the ten first natural frequencies of a 5 span viaduct. If a Bernoulli–Euler beam model is used, the first natural frequency increases noticeably to 13.00 Hz.

Fig. 21 illustrates how the dynamic contribution to the static deformation (static vs dynamic influence lines) varies with the pod velocity for a 10 span tube. Despite the higher absolute displacement obtained in downwards sense, the dynamic amplification is significant during the upwards movement, which influences the positive DAFs. Other pod configurations with two and four axles covering a total distance of 10m have been analysed, and a reduction of dynamic response has been observed; these results are not shown for the sake of brevity.

Fig. 22 shows the DAF computed according to Eq. (28). Considering the most adverse response (*i.e.* with the pod weight acting as a single point load), the maximum displacement DAF is 2.9 for upward displacements, while downwards amplifications are lower and equal to (minus) 1.7. There are no substantial differences in the displacement response when VBI is considered, and the global values are very similar also if a tube with only five spans is analysed. If quarter-span sections are removed and only mid-span sections are considered, the maximum DAF obtained for upwards displacements reduces to 2.6, while for downwards displacements is equal to 1.6. The DAFs obtained in this section confirm that fatigue analysis is not a key concern for a preliminary design. Only for vehicles of weight above 100 kN some refinements to Section 8 would be advisable, in order to use less conservative assumptions.

While for RWB vertical acceleration levels are critical for ballast stability and vehicle comfort, at this stage no conclusive vibration SLS analysis for HL systems can be carried out due to the lack of reliable

Table 8
Natural frequencies of the first ten bending modes of a five-span viaduct (2 clusters).

Mode No. (freq. Hz)									
1	2	3	4	5	6	7	8	9	10
11.82	14.13	16.97	19.44	20.49	38.23	40.62	43.30	45.43	46.25

information about (i) the vibration intensity and frequency content that HL pod guiding systems can withstand without malfunctioning, and (ii) how the vibration will be effectively transmitted to the passengers once suspension systems will be fully developed. Therefore, a simplified analysis is deserved regarding the levels of vibration.

Fig. 23 shows the maximum vertical accelerations among mid-span and quarter-of-span sections of the tube computed with three different models mentioned before. The number of modes is limited to 10 (2 clusters), which entails that frequencies above 50 Hz approx. are disregarded. For RWB a typical cut-off frequency is 30 Hz, but it is not possible for the moment to establish an indisputable cut-off frequency for an SLS assessment of HL infrastructure. Therefore, 50 Hz and 2 clusters are deemed a reasonable first approach. Regarding the vertical accelerations in the pod, the levels are low due to the very small span-to-deflection ratio caused by the vehicle passage (from Fig. 20, $L/\delta \simeq 28/(0.359{\cdot}10^{-3}) \simeq 78000$): maximum accelerations equal to 0.03 m/s^2 have obtained in the pod at speeds $V \leqslant 1200$ km/h.

The sensitivity to the number of spans has been investigated with models up to 80 spans. While the maximum displacement has shown only a small sensitivity, the acceleration curves reveal increases in the peak response at certain speeds, especially at 1050 km/h. These peaks elevate the maximum acceleration up to 30 spans, when convergence is reached. Slightly larger influence of VBI is observed. Such peaks are explained by the spectral content of the excitation force associated to certain modes: for particular pod velocities, higher harmonics of the modal force of some modes are close to its corresponding modal frequency and, for this reason, their resonant amplification arises in the total response. This effect is more prominent for accelerations than for displacements due to squared frequency appearing in the second derivative of the time-dependent modal amplitude. In total, the peak acceleration with cut-off frequency of 50 Hz reaches 2.4 m/s^2. However, it should be born in mind that the results are quite different for a Bernoulli–Euler model, not only because the peaks shift to higher speeds due to the higher frequencies, but also because the shape of the modes varies and the peaks are largely smoothed out.

If simply-supported (S-S) end conditions were considered, the span length of the extreme spans should be reduced, as it is customary in continuous viaducts. Because all practical implications of the end rotations should also be considered, the analysis of such case is outside the scope of the paper. However, since converged results in acceleration are obtained for a large number of spans (30), no determinant variations are expected for S-S end supports.

10. Conclusions

In this article, the design constraints of tubular steel viaducts for Hyperloop have been analysed. It has been assumed that, in addition to serving to install the vehicle's guidance system and as a containment of the necessary vacuum, the tube has also a load-bearing function. A tube diameter of 4 m has been selected as representative. Span lengths ranging from 20 to 40 m and tube thickness values between 20 and 40 mm have been considered. Two basic Configurations have been analysed: (R) the tube is joined to the piers, hence its thermal expansion is elastically restrained; (F) the tube can freely expand. In the R-Configuration, it has been assumed that ring stiffeners are placed at every support cross-section; additionally, instability has been analysed either with no intermediate stiffening between piers, or with two intermediate ring stiffeners. In F-Configuration, since the axial displacements due to expansion can be very large, the existence of stiffeners (not even on supports) has not been contemplated. The steel grade has been generally considered to be S460 (Eurocode). The following conclusions have been obtained:

1. The effect of temperature changes has been studied for the restrained tube (R-Configuration) with a simplified straight bar model with a continuous longitudinal elastic restraint. The analysis shows that the longitudinal expansion can be limited to a desired value by increasing the stiffness per unit length of the support above a value that depends on the axial rigidity of the tube and the magnitude of the temperature increase, and is independent of the length of the structure. Conversely, the maximum pier-structure horizontal interaction force can be limited by keeping the distributed stiffness under a value with the same dependencies as the previous one. A case study considering standard soil conditions showed that the security margin for the horizontal resistance of the foundation in the R-Configuration would be scarce and measures to increase its horizontal stiffness should be taken.
2. Long structures (hundreds of km) with no expansion joints and no restriction to expansion (F-Configuration) would have longitudinal displacements of the order of magnitude of the span lenght, which would require the development of non-standard technological solutions for supports on piers and stations.
3. Critical stresses in the tube under axial compression, bending and vacuum have been preliminarily assessed basing on [20] for the mentioned ranges of span length and thickness. Results show that critical hoop stresses due to vacuum are much lower than the yield stress, whereas critical longitudinal stresses due to axial compression and bending are much higher than the yield stress.
4. A case of a structure in R-Configuration with a span length of 28 m and 25 mm thickness has been studied under standard static Eurocode loads to check the orders of magnitude of the effects of different actions. Buckling analysis was not carried out initially, but postponed instead to a latter section in the paper (Section 7). Stresses due to thermal expansion are, by far, the highest and their magnitude is independent of the section properties; this justifies the selection of S460 steel. The effect of wind is practically negligible, and the vehicle would only be relevant for very high impact factors that have been discarded by the dynamic analysis.
5. Section 7 summarizes the results of the joint static and instability analyses in graphs that provide the allowable impact coefficient for a given diameter. For a R-Configuration tube with no intermediate stiffeners, a minimum thickness of 25 mm is needed; it works for span lengths under 30 m, even for strong impact coefficients. Adding two intermediate ring stiffeners allows 20 mm tubes for span lengths under 35 m. However, graphs show that reducing the sensitivity to buckling would require higher thickness values. F-Configuration, having no ring stiffeners because of the large longitudinal movements, requires at least 30 mm thickness, although the absence of longitudinal stresses due to thermal expansion could allow lower steel grades.
6. With the conservative hypotheses adopted in this work, fatigue is not a concern for vehicles of weight below 100 kN. Since some of the hypotheses adopted could be substituted by less conservative ones for a refined analysis, fatigue would probably not be relevant either for heavier pods.
7. The dynamic impact factor (DAF) has been computed based on the vertical displacements. For the case study mentioned in the preceding conclusions, its values are relatively low compared with what was anticipated by previous publications. It should be remarked that the critical speed predicted for the fundamental mode is above 2000 km/h; such critical speed is a result of the high fundamental bending frequency —close to 12 Hz—, which, in turn, comes out from the stiffness requirements derived from the previous static and stability analyses. Despite the higher absolute displacement obtained in downward sense, the dynamic response is also significant during the upwards movement. This is also identified in the impact factor curves, leading to even higher *positive* DAFs due to the lower upwards static values. Impact factor increases only slightly with the number of spans. Besides, vehicle-structure interaction has not a significant influence for the adopted, simplified vehicle idealisation.

8. Preliminary accelerations analyses, despite the lack of reliable information about the pod suspension, reflect that acceleration levels in the pod are low due to the small span-to-deflection ratio caused by the vehicle passage. As for the vibrations of the tube, the maximum level is moderate, but the number of spans and modes included in the simulation is relevant. Convergence in the vertical accelerations has been achieved in this study with models of 30 spans for frequencies up to some 50 Hz, with no strong sensitivity to be expected regarding the end support conditions for such a number of spans. Even if the critical velocity for the fundamental mode is far from being reached, resonance phenomena are observed for some of the higher harmonics of certain mode shapes, leading to peak values of 2.4 m/s^2; this phenomenon is significantly reduced if Bernoulli–Euler beam theory is adopted, which paves the way for future investigations.

Declaration of Competing Interest

The authors declare that they have no known competing financial interests or personal relationships that could have appeared to influence the work reported in this paper.

Acknowledgements

The authors gratefully acknowledge the financial support of the *Generalitat Valenciana*, through grant AICO/2019/025 for the project "Análisis Dinámico aplicado al Diseño de Viaductos para Hyperloop: Vibraciones de Flexión, Torsión y Límites Normativos", within research funding program AICO2019: *Subvenciones para grupos de investigación consolidables*.

Appendix A. Solutions of the restrained expansion problem

A.1. Uniform temperature increment

In this case $\epsilon_T = \alpha T_u$ is constant. Therefore, the independent term of Eq. (4) is null and the field equation is homogeneous:

$$\frac{\mathrm{d}^2 u}{\mathrm{d}x^2} - \frac{k}{EA}\,u(x) = 0 \tag{A.1}$$

The general solution is

$$u(x) = C_1 \exp\left(\sqrt{\frac{k}{EA}}\,x\right) + C_2 \exp\left(-\sqrt{\frac{k}{EA}}\,x\right) \tag{A.2}$$

Placing the origin in the centre of the bar, a first boundary condition is $u(0) = 0$. It follows that $C_1 + C_2 = 0$, and the solution becomes

$$u(x) = 2\,C_1 \sinh\left(\sqrt{\frac{k}{EA}}\,x\right) \tag{A.3}$$

The second boundary condition (free end) is $N(L) = 0$. To apply it, we evaluate the interaction force using (3)

$$f(x) = -2\,k\,C_1 \sinh\left(\sqrt{\frac{k}{EA}}\,x\right) \tag{A.4}$$

and integrate it to get the axial force:

$$N(x) = N(0) + 2\,k\,C_1 \sqrt{\frac{EA}{k}} \cosh\left(\sqrt{\frac{k}{EA}}\,x\right) \tag{A.5}$$

Plugging (A.3) and (A.5) into (2) yields

$$N(0) = -EA\,\alpha T_u \tag{A.6}$$

Hence, the condition $N(L) = 0$ results in

$$C_1 = \frac{1}{2}\alpha T_u \sqrt{\frac{EA}{k}}\,\frac{1}{\cosh\left(L\sqrt{\frac{k}{EA}}\right)} \tag{A.7}$$

Defining the elastic slenderness as

$$\lambda_k = L\sqrt{\frac{k}{EA}} \tag{A.8}$$

and introducing the non-dimensional variable $\xi = x/L$, the solution is

$$u(\xi) = \alpha T_u L\,\frac{1}{\lambda_k}\,\frac{\sinh(\lambda_k\,\xi)}{\cosh(\lambda_k)} \tag{A.9}$$

A.2. Uniform temperature gradient between tube ends

Assuming a longitudinal temperature gradient from $-T_a$ at $x=-L$ to T_a at $x=L$, the strain due to temperature is

$$\epsilon_T(x)=\alpha T_a\frac{x}{L} \tag{A.10}$$

and the solution of (4) is

$$u(x)=-\alpha\frac{T_a}{L}\frac{EA}{k}+C_1\exp\left(\sqrt{\frac{k}{EA}}x\right)+C_2\exp\left(-\sqrt{\frac{k}{EA}}x\right) \tag{A.11}$$

Therefore, the interaction force becomes

$$f(x)=\frac{EA\,\alpha T_a}{L}-C_1\,k\exp\left(\sqrt{\frac{k}{EA}}x\right)-C_2\,k\exp\left(-\sqrt{\frac{k}{EA}}x\right) \tag{A.12}$$

Integration of the interaction force provides the axial force:

$$\begin{aligned}N(x)&=N(0)-EA\,\alpha T_a\frac{x}{L}\\&+C_1\,k\sqrt{\frac{EA}{k}}\left(\exp\left(\sqrt{\frac{k}{EA}}x\right)-1\right)-C_2\,k\sqrt{\frac{EA}{k}}\left(\exp\left(-\sqrt{\frac{k}{EA}}x\right)-1\right)\end{aligned} \tag{A.13}$$

In this skew-symmetric case, $N(-L)=N(0)=N(L)=0$; the integration constants follow from these conditions:

$$C_1=C_2=\frac{1}{2}\alpha T_a\sqrt{\frac{EA}{k}}\,\frac{1}{\sinh\left(L\sqrt{\frac{k}{EA}}\right)} \tag{A.14}$$

Finally, the solution for the displacements in terms of dimensionless parameters is

$$u(\xi)=\alpha T_a L\left(\frac{1}{\lambda_k}\frac{\cosh(\lambda_k\xi)}{\sinh(\lambda_k)}-\frac{1}{\lambda_k^2}\right) \tag{A.15}$$

and the interaction forces and axial forces become

$$f(\xi)=-k\,u(\xi)\qquad N(\xi)=-EA\,\alpha T_a\left(\xi-\frac{\sinh(\lambda_k\xi)}{\sinh(\lambda_k)}\right) \tag{A.16}$$

Appendix B. Evaluation of the horizontal stiffness and soil strength of a typical pier-foundaton system

In this appendix, we study the horizontal stiffness and soil strength corresponding to a typical (notional) pier-foundation system of a viaduct in R-Configuration. An average span width of $l=30$ m is assumed. The viaduct is supported on reinforced concrete piers with pile foundations on medium-compact clay. The following specific assumptions have been made (see Fig. 24): (1) piers of reinforced concrete ($E_c=30$ GPa) have a 3.5 m (in transverse direction) × 1.5 m rectangular cross section and are 7 m high; (2) the bottom face of the pile cap is 2.5 m deep, and the groundwater level is assumed to coincide with it; (3) reinforced concrete piles (same Young's modulus as piers) are 15 m long with a diameter of 1.2 m with a separation equal to 3.6 m in both directions; (4) the typical pile cluster is composed of 3 × 3 piles; (5) the clay is normally consolidated, with dry specific weight $\gamma=18$ kN/m^3, submerged specific weight $\gamma'=10$ kN/m^3 and plasticity index $IP=50$.

The undrained shear strength of the soil can be estimated according to Skempton [36,37] as $s_u=(0.11+0.0037\cdot IP)\sigma'_{v0}$. Therefore, the average undrained shear strength can be calculated with the vertical effective stress at a depth $z=2.5+15/2=10$ m : $\sigma'_{v0}=18\cdot2.5+10\cdot(10-2.5)=120$ kN/m2. Hence, $s_u=35.4$ kN/m^2.

With these data, the horizontal stiffness of the pile cluster has been evaluated according to [38, Chapt. 3.4]. Firstly, the horizontal stiffness of a single pile is given by

$$K_h=\left(0.68+0.20\ln\frac{l_p}{l_{el}}\right)\frac{EI_p}{l_{el}^3}\leqslant\frac{EI_p}{l_{el}^3} \tag{B.1}$$

where EI_p is the section stiffness of the pile, l_p is the pile length and $l_{el}=(EI/(75s_u))^{1/4}$ is the elastic length. For the given data

$$l_{el}=5.82\text{ m},K_h=13440\text{ kN/m} \tag{B.2}$$

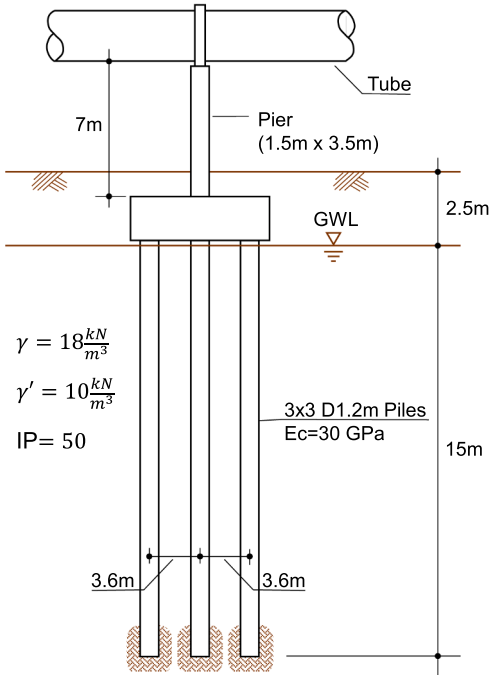

Fig. 24. Sketch of a typical pier and its foundation.

For the cluster, elastic lengths need to be corrected using a coefficient η defined as follows

$$\eta = 1 + 0.5\left(d_p/s_x\right)^2 \leqslant 1.1 \text{ (first row)} \tag{B.3}$$

$$\eta = \left(1 + 0.5\left(d_p/s_x\right)^2\right)\left(1 + \left(d_p/s_y\right)^2\right) \leqslant 1.3 \text{ (other rows)} \tag{B.4}$$

where d_p is the pile diameter and s_x, s_y are the separations in both directions. The total stiffness is the sum of every stiffness calculated with the corresponding corrected elastic length ηl_{el}.

The result, for $s_x = s_y = 3.6$ m, is $K_{h,foundation} \approx 82000$ kN/m which provides a group efficiency of 0.678. The pier horizontal stiffness is $K_{h,pier} = 3EI_c/h^3 = 258291$ kN/m, with EI_c, flexural rigidity, and h, height of the pier. In conclusion, the horizontal stiffness of the pier-foundation system is $K = (1/K_{h,foundation} + 1/K_{h,pier})^{-1} \approx 62240$ kN/m.

Regarding the horizontal strength of soil, reference [39] provides the lateral failure load for a single pile, $F_{hu} = \zeta s_u d_p^2$, with the coefficient $\zeta \approx 30$ for the given data. That leads to $F_{hu} = 1529$ kN. The failure load for the cluster can be calculated using the previously obtained efficiency, $F_{hu,foundation} = 0.678 \cdot 9 \cdot 1529 = 9331$ kN.

References

[1] Musk E. Hyperloop Alpha, SpaceX; 2013. https://www.spacex.com/sites/spacex/files/hyperloop_alpha.pdf.

[2] Great Lakes Hyperloop: Feasibility Study, Tech. rep., Transportation Economics and Management Systems Inc, prepared for Northeast Ohio Areawide Coordinating Agency in Cooperation with Hyperloop Transportation Technologies, Inc.; 12 2019.

[3] The biggest challenges that stand in the way of Hyperloop, Interesting Engineering; 2017. https://interestingengineering.com/biggest-challenges-stand-in-the-way-of-hyperloop.

[4] Un total de 15 organizaciones se inscriben en un grupo de trabajo que busca la estandarización del sistema Hyperloop, 2019/07/02 - Europa Press/ Andalucía; 2019.

[5] UNE promotes the future development of European standards for hyperloop systems, 2020/02/14 - UNE; 2020. https://tinyurl.com/sg2zru5.

[6] Global Hyperloop Technology Market Size, Status and Forecast 2019–2025, Tech. rep., Reports and Markets; 5 2019.

[7] Concept study province North-Holland, Tech. rep., Hyperloop Hardt and Province North-Holland; 4 2020. https://hardt.global/sub/press/hyperloopstudynoord-holland/.

[8] Germany scraps Transrapid rail plans, 2008/03/27 - DW (German News Service); 2008. https://p.dw.com/p/DVSA.

[9] Initial order of magnitude analysis for Transpod Hyperloop system infrastructure: Preliminary basis of design, Tech. rep., Transpod; 2017.

[10] Alexander NA, Kashani MM. Exploring bridge dynamics for ultra-high-speed, hyperloop, trains. Structures 2018;14:69–74. https://doi.org/10.1016/j.istruc.2018.02.006.

[11] Ahmadi E, Alexander NA, Kashani MM. Lateral dynamic bridge deck-pier interaction for ultra-high-speed hyperloop train loading. Proc Inst Civil Eng-Bridge Eng 2020;173(3): 198–206. doi:10.1680/jbren.19.00011.

[12] Connolly DP, Alves Costa P. Geodynamics of very high speed transport systems. Soil Dynam Earthquake Eng 2020;130: 105982. doi:10.1016/j.soildyn.2019.105982.

[13] Yan B, Dai GL, Hu N. Recent development of design and construction of short span high-speed railway bridges in China. Eng Struct 2015;100:707–17. https://doi.org/10.1016/j.engstruct.2015.06.050.

[14] Nick N, Sato Y. Computational fluid dynamics simulation of hyperloop podpredicting laminar-turbulent transition. Railway Eng Sci 2020;28(1):97–111. https://doi.org/10.1007/s40534-020-00204-z.

[15] TMR Stainless, Practical Guidelines for the Fabrication of Duplex Stainless Steel, Tech. rep., International Molybdenum Association; 2014.

[16] EN 1993-1-6:2007, Eurocode 3: Design of steel structures - Part 1–6: Strength and stability of shell structures, Tech. rep., The European Union; 2007.

[17] EN 1991-1-5:2003, Eurocode 1: Actions on Structures - Part 1–5: General actions - Thermal actions, Tech. rep., The European Union; 2003.

[18] Brush Don O, Almroth Bo O. Buckling of Bars. Plates and Shells: McGraw-Hill; 1975.

[19] González A. Una revisión user friendly del ecosistema hyperloop y sus posibilidades de convertirse en el quinto medio de transporte humano., Blog – Angels Capital; 2019. https://www.angelscapital.es/hyperloop-el-transporte-del-futuro.

[20] NASA. SP-8007, Buckling of Thin-Walled Circular Cylinders, Tech. rep., NASA Space Vehicle Design Criteria (Structures). National Aeronautics and Space Administration 1968.
[21] Davis S. Watch: World's first full-sized Hyperloop capsule unveiled in Spain, 2018/10/04 - Euronews; 2018.
[22] EN 1991-1-4:2005, Eurocode 1: Actions on Structures - Part 1–4: General actions - Wind actions, Tech. rep., The European Union; 2005.
[23] EN 1990:2002+A1, Eurocode: Basis of Structural Design, Tech. rep.; 2010.
[24] EN 1991–2:2003, Eurocode 1: Actions on structures - Part 2: Traffic loads on bridges, Tech. rep., The European Union; 2003.
[25] Roark Raymond J, Young Warren C, Budynas Richard G. Roark's formulas for stress and strain. McGraw-Hill; 2002.
[26] Dudnikov EE. Structure of hyperloop systems with intermediate station. In: Tsvirkun A, editor. Proceedings of 2019 Twelfth International Conference 'Management of large-scale system development' (MLSD), IEEE; 2019. doi:10.1109/MLSD.2019.8911040.
[27] EN 1993-1-9:2005, Eurocode 3: Design of steel structures - Part 1–9: Fatigue, Tech. rep., The European Union; 2005.
[28] EN 1993–2:2006, Eurocode 3: Design of steel structures - Part 2: Steel bridges, Tech. rep., The European Union; 2006.
[29] Hayashikawa T, Watanabe N. Dynamic behavior of continuous beams with moving loads. J Eng Mech Divis, ASCE 1981;107:229–46.
[30] Wang R. Vibration of multi-span Timoshenko beams to a moving force. J Sound Vib 1997;207(5):731–42.
[31] Johansson C, Pacoste C, Karoumi R. Closed-form solution for the mode superposition analysis of the vibration in multi-span beam bridges caused by concentrated moving loads. Comput Struct 2013;119:85–94.
[32] Martínez-Castro A, Museros P, Castillo-Linares A. Semi-analytic solution in the time domain for non-uniform multi-span Bernoulli-Euler beams traversed by moving loads. J Sound Vib 2006;294:278–97.
[33] Anicotte C, Schmitt P. Dynamic study of railway bridges under new reference load models for Multiple Units. Tech. rep., SNCF, Direction of Engineering, Dpt. of Structures 2012.
[34] Doménech A, Museros P, Martínez-Rodrigo M. Influence of the vehicle model on the prediction of the maximum bending response of simply-supported bridges under high-speed railway traffic. Eng Struct 2014;72:123–39. https://doi.org/10.1016/j.engstruct.2014.04.037.
[35] Cantero D, Arvidsson T, OBrien E, Karoumi R. Train-track-bridge modelling and review of parameters, Struct Infrastruct Eng; 2015. doi:10.1080/15732479.2015.1076854.
[36] Skempton AW. Discussion: Sensitivity of clays and the c/p ratio in normally consolidated clays. Proc Am Soc Civil Eng Separ 1954;478:19–22.
[37] Skempton AW. Discussion: Further data on the c/p ratio in normally consolidated clays. Proc Inst Civ Eng 1957;7:305–7.
[38] Jiménez Salas JA. Geotecnia y Cimientos III (in Spanish). Madrid: Editorial Rueda; 1980.
[39] Broms Bengt B. Lateral resistance of piles in cohesive soils. J Soil Mech Found Divis ASCE 1964;90(2):27–63.